DIPLOMARBEIT

Untersuchung von 3D-Konfigurationen für Bildgebungsverfahren der Spektralen Induzierten Polarisation

zur Erlangung des akademischen Grades

Diplom-Ingenieur

im Rahmen des Studiums

Geodäsie und Geoinformation

eingereicht von

Clemens Moser

Matrikelnummer 01602882

ausgeführt am Department für Geodäsie und Geoinformation
der Fakultät für Mathematik und Geoinformation der Technischen Universität Wien

Betreuung
Betreuer: Prof. Dr. Adrian Flores-Orozco
Mitwirkung: Prof. Dr. Andrew Binley

Wien, 09.02.2023

(Unterschrift Verfasser)

(Unterschrift Betreuer)

Erklärung zur Verfassung der Arbeit

Clemens Moser

Hiermit erkläre ich, dass ich diese Arbeit selbständig verfasst habe, dass ich die verwendeten Quellen und Hilfsmittel vollständig angegeben habe und dass ich die Stellen der Arbeit – einschließlich Tabellen, Karten und Abbildungen –, die anderen Werken oder dem Internet im Wortlaut oder dem Sinn nach entnommen sind, auf jeden Fall unter Angabe der Quelle als Entlehnung kenntlich gemacht habe.

Wien, 09.02.2023

Clemens Moser

Danksagung

Die vorliegende Diplomarbeit wurde im Forschungsbereich Geophysik am Department für Geodäsie und Geoinformation der TU Wien verfasst. Zuallererst möchte ich mich bei meinem Betreuer Prof. Adrian Flores-Orozco bedanken, nicht nur für die unzähligen Ideen, Verbesserungsvorschläge und Gespräche, die in die vorliegende Arbeit eingeflossen sind, sondern auch dafür, dass du mir die Mitarbeit bei einer Vielzahl an Projekten ermöglicht hast, durch die ich unheimlich viel dazulernen konnte. Weiters möchte ich Prof. Andrew Binley danken, der mit der Bereitstellung seines Inversionsalgorithmus ResIPy sowie mehrmaliger Online-Gespräche, schriftlicher Korrekturen und Verbesserungsvorschlägen meine Diplomarbeit unterstützt hat.

Für die Unterstützung bei den Feldmessungen möchte ich mich ganz besonders bei Raphael Vasak, Franziska Öhlinger, Nathalie Roser und Anna Hettegger bedanken. Weiters gilt mein Dank Walter Loderer, der bei technischen Problemen immer eine Lösung parat hat.

Zudem bedanke ich mich beim Umweltbundesamt für die Unterstützung Zugang zu den Deponien Heferlbach und Kappern zu erhalten.

Zuletzt möchte ich mich auch bei Lena bedanken, für deine Fähigkeit mich in den richtigen Momenten abzulenken, und bei meiner Familie, für eure Begleitung und Unterstützung während meines gesamten Studiums.

Kurzfassung

3D-Verfahren der Induzierten Polarisation (IP) werden gewöhnlich unter Verwendung paralleler 2D-Elektrodenlinien mit Messungen innerhalb der einzelnen Linien durchgeführt. Die Anwendung solcher Messkonfigurationen führt jedoch zu einer verringerten Auflösung zwischen den Linien, was besonders im Falle heterogen verteilter elektrischer Eigenschaften im Untergrund, wie z.B. in Deponien, kritisch ist. Um derartige Probleme zu vermeiden, wird im Rahmen dieser Arbeit untersucht, wie 3D-Konfigurationen die Auflösung bei Messungen der Spektralen IP verbessern können, genauer gesagt wurde untersucht wie gut verschiedene 2D- und 3D-Elektrodenkonfigurationen bei Verfahren der Einzel- und Multi-Frequenz IP die elektrischen Eigenschaften des Untergrundes wiedergeben können. Dazu wurden zuerst Unterschiede zwischen parallelen 2D-Linien und zwei 3D-Konfigurationen mithilfe einer numerischen Modellierung herausgearbeitet. Als 3D-Konfigurationen wurden eine Grid-Konfiguration, bei der die Elektroden in einem quadratischen Raster angeordnet wurden, sowie eine Kreis-Konfiguration, bei der die Elektroden in vier konzentrischen Kreisen angeordnet wurden, untersucht. Um die Konfigurationen unter richtigen Feldbedingungen zu testen, wurden im nächsten Schritt Messungen mit den 2D- und 3D-Konfigurationen in zwei Deponien durchgeführt. Sowohl die Ergebnisse der numerischen Modellierung als auch die Ergebnisse der Feldmessungen zeigen, dass sich bei Messungen mit den parallelen 2D-Linien Artefakte und eine verringerte Auflösung im resultierenden 3D-Modell bilden, besonders im Falle polarisierbarer Anomalien. Im Gegensatz dazu zeigen die Ergebnisse der numerischen Modellierung und der Felddaten, dass 3D-Konfigurationen IP-Anomalien gut detektieren können und tragen so zu einer Verbesserung der Abschätzung der räumlichen Verbreitung von Müll bei. Weiters zeigen die Ergebnisse, dass die Raster-Konfiguration mit Messungen über Elektrodenlinien hinweg und verschiedenen Dipolrichtungen bessere Ergebnisse liefert als die Kreis-Konfiguration, die im Zentrum ihrer konzentrischen Kreise eine verringerte Auflösung aufweist. Zusätzliche Untersuchungen der Frequenzabhängigkeit der synthetischen Daten und der Felddaten zeigen, dass 3D-Konfigurationen stabilere Spektren der komplexen Leitfähigkeit liefern als 2D-Konfigurationen. Stabile Spektren sind für eine genaue Schätzung von Parametern, die die Frequenzabhängigkeit beschreiben (z.B. Cole Cole), nötig.

Abstract

3D induced polarization (IP) surveys are commonly conducted by using a series of parallel 2D electrode lines with collinear measurements. However, such measurements are limited in the resolution between the lines which is critical in the case of highly heterogeneous subsurface conditions, such as in landfills. To overcome this, we investigate here the enhanced resolution in spectral IP (SIP) measurements through 3D imaging measurements, i.e., we investigate the resolving capabilities of different electrode configurations for 3D single- and multi-frequency IP surveys. First, we investigate, through a numerical study, the difference between results from using 2D parallel collinear electrode arrays and true 3D configurations. In particular for 3D settings, we investigate (1) a grid array with electrodes set in a quadratic mesh, and (2) a circular array with electrodes set in four concentric circles. Second, we collected SIP data using 2D and 3D configurations in two landfills to evaluate the application of our results in real field conditions. Both the numerical and the field experiments demonstrate that measurements of parallel 2D collinear arrays result in the creation of artifacts and the loss of resolution in the 3D structure, especially of polarizable features. In contrast, the two 3D configurations are able to resolve IP anomalies in synthetic simulations and in the field trials, resulting in a better delineation of the geometry of waste units. Furthermore, our results show that the 3D grid array with crossline measurements and multiple dipole orientations provides better results than the 3D circular array, as the latter lacks resolution in the central area of the survey region. Additional investigations of the frequency-dependence of the synthetic and field data demonstrate that 3D configurations provide more stable spectra of the conductivity magnitude and phase than 2D configurations, which is essential for an accurate estimation of relaxation (e.g., Cole Cole) parameters.

Inhaltsverzeichnis

Abbildungsverzeichnis

Tabellenverzeichnis

1 Introduction

1.1 The induced polarization method in landfills

The induced polarization (IP) imaging method is an extension of electrical resistivity tomography (ERT) (for an overview see e.g., Kemna et al., 2012; Binley and Slater, 2020). The IP method provides a measure of both the electrical conductive and capacitive properties of the subsurface with several studies revealing the sensitivity of these to textural parameters (e.g., Revil et al., 2017; Weller et al., 2010), geochemical properties (e.g., Slater et al., 2007; Flores Orozco et al., 2020) and hydrogeological properties (e.g., Binley et al., 2005; Weller et al., 2015; Revil et al., 2021). Built on such links, field investigations have demonstrated the potential of the IP method in environmental investigations, such as the understanding of the driving forces of landslides (Revil et al., 2020; Flores Orozco et al., 2022; Gallistl et al., 2022), as well as the distribution and transport of groundwater contaminants (e.g., Cassiani et al., 2009; Flores Orozco et al., 2012a; Slater et al., 2010; Bording et al., 2019). There is also growing interest on the application of the IP method on the field to understand geochemical and microbially-mediated processes in the subsurface (Atekwana and Atekwana, 2010; Flores Orozco et al., 2011; McAnallen et al., 2018; Katona et al., 2021).

One of the main environmental applications of the IP method is the investigation of landfills (Iliceto and Morelli, 1999; Johansson et al., 2007; Dahlin et al., 2010). To characterize the internal state of landfills, approaches nowadays typically combine direct methods (i.e., chemical analysis of gas, waste and leachate samples) and geophysical measurements (for a review see Nguyen et al., 2018). ERT has become a well-established method for the delineation of the landfill geometry (Chambers et al., 2006; Soupios et al., 2007; Maurya et al., 2017; Di Maio et al., 2018), as well as for the estimation of the water content (Steiner et al., 2022) and the identification of leachate plumes (Clément et al., 2010; De Carlo et al., 2013; Bichet et al., 2016; Maurya et al., 2017). The IP method has been used to improve the delineation of the waste unit(s) in landfills (Johansson et al., 2007; Dahlin et al., 2010; Nguyen et al., 2018), considering the strong contrast between waste (commonly associated with a high electrical polarization) and the host geology (commonly with a relatively low polarization characteristic) (e.g., Leroux et al., 2007; Frid et al., 2017).

Understanding the landfill composition is important as the anaerobic degradation of organic waste produces methane, which is not only responsible for about 5% of the global greenhouse gas emissions (Lou and Nair, 2009) but also poses a direct threat for surrounding areas because of its potential to cause fires and explosions (Christophersen and Kjeldsen, 2001). Recently, Flores-Orozco et al. (2020) demonstrated the possibility to map areas with high methane production in municipal solid waste (MSW) (i.e, biogeochemically active zones) due to the association with a high polarization characteristic. The authors revealed a lineal correlation between the polarization response and the total organic carbon (TOC), which in turn is linked to high methane production.

Single-frequency IP results in landfills can lead to ambiguities in the interpretation of waste types due to different possible polarization mechanisms acting in different waste types. Gazoty et al. (2012) demonstrated the potential of using the frequency dependence of the complex conductivity to improve the discrimination of different waste types, i.e., they used the characteristic relaxation time to discriminate between areas of metal deposits and areas with sludge and coal.

1.2 2D versus 3D resistivity and IP surveys

The studies mentioned above have revealed the complexity of landfill geometries, for instances regarding spatial variability of the geometry of waste units (e.g., Dahlin et al., 2010), geochemical composition (e.g., Flores Orozco et al., 2021) and water content (e.g., Steiner et al., 2022). Nonetheless, to-date, IP investigations in landfills have been primarily conducted using 2D measurements, i.e., with data collected along collinear electrode arrays, with the imaging plane representing electrical variations collected along each line. 2D measurements are well-suited in those cases where the subsurface properties are nearly homogeneously distributed perpendicular to the direction of the electrode line (Bentley and Gharibi, 2004; Chambers et al., 2002; Van Hoorde et al., 2017; Nimmer et al., 2008) and allow deep investigations (favored by long separation between current and potential dipoles) as well as high spatial resolution (favored by small electrode spacing). By using independent 2D lines, mapping extensive areas permits flexibility, e.g., moving electrode positions or entire electrode arrays due to obstacles; they also allow the use of simple electrode configurations and minimal computer resources for 2D modeling and inversion. Adopting such survey strategies, the calculation of geophysically anomalous subsurface volumes (e.g., representing waste units) requires the interpolation of 2D inversion results (e.g., Gazoty et al., 2012; Wainwright et al., 2016; Katona et al., 2021). In contrast, 3D measurements require extensive field effort (Van Hoorde et al., 2017), can cover only smaller areas by using the same number of electrodes (Dahlin and Bernstone, 1997) and require significantly more computer resources during the processing of the data (e.g., Johnson et al., 2010).

The main drawback of 2D ERT and IP surveys is the poor sensitivity of the resulting model in the area between the profiles, which might mislead the interpretation of the results (Chambers et al., 2002). This issue is especially critical for complex subsurface conditions such as landfills where spatial variations of the electrical properties are expected in all directions. Moreover, in 2D surveys, topographical changes perpendicular to the profile direction are typically ignored within the inversion, although they may influence the inversion result, especially in cases of complex terrain (Bièvre et al., 2018). The only way to account for heterogeneous electrical properties and strong topographical changes is through three-dimensional modeling and inversion, which is often used in hydrogeological resistivity investigations (e.g., Chambers et al., 2007; Chambers et al., 2012; Auken et al., 2014; Johnson et al., 2015; Wilkinson et al., 2016; Soueid Ahmed et al., 2018). Chambers et al. (2002) demonstrated that three-dimensional modeling and inversion is also essential for IP surveys. The authors conducted time-domain IP measurements along parallel 2D lines and inverted the data two-dimensionally (merged for quasi-3D model) and three-dimensionally (3D model). Only 3D modeling correctly recovered an IP anomaly (metal drum) in the subsurface, while the quasi-3D model revealed images strongly affected by artifacts.

In both ERT and IP surveys, a quasi-3D model can be resolved through the 3D inversion of a series of parallel 2D collinear arrays to still allow 3D coverage but avoiding a number of constraints related to true 3D surveys (e.g., Dahlin et al., 2002a; Aizebeokhai and Singh, 2013; Auken et al., 2014; Abdulsamad et al., 2019). Cheng et al. (2019) illustrates the same approach for a series of non-parallel 2D surveys. However, as mentioned above, collecting data along 2D collinear arrays limits to resolve structures between the survey lines (Dahlin et al., 2002a; Dahlin and Bernstone 1997; Chambers et al., 2002). Loke and Barker (1996) proposed the application of 2D rectangular (in plan) electrode arrays to measure in at least one additional direction. Chambers et al. (2002) explored the value of orthogonal survey lines (in true 3D and quasi-3D configurations) to delineate the structure of narrow buried walls.

To obtain resistivity information about the subsurface beneath surface features such as buildings, Argote-Espino et al. (2013) developed 3D shaped configurations, such as the L-Corner array, which is based on quadrupoles along and across four perpendicular lines. In comparison to several parallel or rectangular 2D lines, which are commonly used, such arrays are limited by a low sensitivity in the shallow central area, because the central area is far away from the electrodes (Tejero-Andrade et al., 2015). A simple true 3D ERT survey configuration commonly used (e.g., Auken et al., 2014; Johnson et al., 2015; Boyd et al., 2021) consists of parallel lines with measurements splitting the dipoles within two lines, i.e., injecting current along two electrodes of the current line and measuring the potential along two electrodes of a different potential line. Dahlin and Bernstone (1997) and Van Hoorde et al. (2017) developed a 3D roll along system consisting of several parallel 2D lines with measurements between every possible line pair (crossline), where one line is used for current injection and one line for potential measurements. Brunner et al. (1999) distributed 72 electrodes along three concentric lines (with a radius of 200, 400 and 875 m), permitting the use of many dipole orientations, to investigate a deep maar (500 m depth of investigation reach). Tsourlos et al. (2014) demonstrated an improved resolution with measurements collected over parallel concentric lines for the characterization of a tumulus, whereby the lines were set symmetrically around the tumulus. Nyquist and Roth (2005) proposed the use of circle-shaped quadrupoles in a configuration of rectangular lines.

1.3 Objectives

Although the main observations regarding signal-to-noise ratio (S/N) or resolution can be extrapolated from 3D ERT to 3D IP surveys, variations in the signal strength of polarization measurements and particular sources of error (e.g., electrode polarization and electromagnetic coupling) need to be taken into account for the design of a 3D IP configuration. While several studies have shown the advantages of 3D surveys over 2D surveys for resistivity investigations, only Chambers et al. (2002) demonstrated that 3D modeling improves the reconstruction quality of a polarizable anomaly over 2D modeling. Thus, in this study we investigate the resolving capabilities of different 2D and 3D electrode configurations for single- and multi-frequency IP surveys. In a first step, we present single-frequency imaging results of numerical (synthetic) modeling experiments aiming at evaluating the reconstruction quality of different 3D configurations. In a second step, we present results for 3D single-frequency field data collected in two landfills, allowing us to investigate signal strength and data error issues in real environments. Furthermore, we investigate the influence of 2D and 3D measurements in the recovered frequency-dependence of multi-frequency synthetic and field IP data. We demonstrate that the geometry and volume of IP anomalies and the frequency-dependence of the IP can be resolved more accurately by using 3D configurations with more than one dipole orientation than measurements collected through parallel 2D electrode lines. The field data were collected on a municipal solid waste and a construction and demolition waste (CDW) landfill, corresponding to high and low polarization responses, respectively.

This master thesis will be submitted to an international geophysical journal with the following title: 3D electrode configurations for spectral induced polarization surveys in landfills. (Authors: Clemens Moser, Andrew Binley, Adrian Flores Orozco)

2 Material and Methods

2.1 The frequency-domain induced polarization method

The IP method is an extension of the resistivity method, which provides a measure of the electrical conductivity and capacitive properties of the subsurface (Binley and Slater, 2020). The method is based on a 4-electrode array where two electrodes are used to inject current, while two additional electrodes measure the resulting electric voltage (Ward, 1990). IP measurements can be conducted in the time- or frequency-domain. Time-domain IP (TDIP) measurements consist of a transfer resistance and an integral chargeability (based on sampling of the secondary voltage after switching off the applied current). Frequency-domain IP (FDIP) measurements provide a transfer impedance (Z^*) in terms of the magnitude $|Z^*|$ (given by the voltage to current ratio, also the resistance) and the phase-shift between voltage and current (φ):

$$Z^* = |Z^*|e^{i\varphi} \tag{1}$$

Inversion of hundreds to thousands of measurements with different 4-electrode combinations results in the distribution of the complex conductivity (σ^*) - or its inverse the complex resistivity (ρ^*). The in-phase, or real component (conductivity, σ') describes the conductive properties (energy loss), while the quadrature, or imaginary component (polarization, σ'') represents the capacitive properties (energy storage). The complex conductivity can also be expressed in terms of its magnitude ($|\sigma^*|$) and its phase (φ):

$$\sigma^* = \sigma' + i\sigma'' = |\sigma^*|e^{i\varphi} \tag{2}$$

Alternatively, the complex conductivity can be represented by its inverse, the complex resistivity ($\rho^* = 1/\sigma^*$). The low conductivity phase values measured in geophysical applications (below 1 rad) (e.g., Binley and Slater, 2020) result in conductivity magnitude values equal to the in-phase conductivity ($|\sigma^*| \approx \sigma'$), the conductivity phase can be approximated to the ratio of the imaginary-to-real component ($\sigma''/\sigma' \approx \varphi$) and the conductivity magnitude is equal to the real part ($|\sigma^*| \approx \sigma'$). Note that we adopt throughout the complex conductivity convention for phase angle φ, i.e., a positive value implies a capacitive effect (for a review of the method see Binley and Slater, 2020 and references therein).

IP measurements at different frequencies are called spectral induced polarization (SIP) or multi-frequency IP and permit to investigate the frequency-dependence of the complex conductivity. The frequency-dependence can be analyzed according to various relaxation models, the most common being the adaption by Pelton et al. (1978) of the Cole Cole (CC) model, which can be written in terms of the conductivity:

$$\sigma^* = \sigma_\infty \left(1 - \frac{M}{1 + (i\omega\tau)^c}\right) \tag{3}$$

where M is the chargeability (dimensionless), defined as $M = \sigma_\infty - \sigma_0$. σ_∞ and σ_0 represent the conductivity at high frequency and low frequency respectively. $i = \sqrt{-1}$ is the imaginary number, ω the angular frequency ($\omega = 2\pi f$), τ represents the relaxation time as the inverse of the critical frequency f_{crit} ($\tau = 1/2\pi f_{crit}$) and c (dimensionless) describes the broadness of the spectrum. Such a phenomenological model lacks a mechanistic link to physical properties of materials and is not adequate in case that the signatures reveal more than one phase maximum (e.g., Nordsiek et al., 2008). However, it represents the simplest expression to describe the SIP response characterized by a dispersion model around the critical frequency (at which the maximum conductivity phase value is observed).

Current conduction in the subsurface can be caused by three mechanisms: (1) The matrix conduction (σ_m) through solid materials, which is negligible in the absence of electrical conductors and semi-conductors such as metals; (2) the electrolytic conduction (σ_f) through fluid-filled pores; (3) and the surface conduction (σ_s) along the electrical double layer (EDL) formed at the interface between particles and pore water (Binley and Slater, 2020).

$$\sigma' = \sigma_m + \sigma_f + \sigma'_s \tag{4}$$

The electrolytic conduction mechanism is controlled by the fluid conductivity, the formation factor describing the pore space geometry (Archie, 1942), and porewater saturation (Binley and Slater, 2020), while the surface conduction is controlled by the surface area and surface charge of the EDL (see further details about the EDL in Schurr, 1964; Waxman and Smits, 1968). Accordingly, the electrical conductivity is commonly expressed as:

$$\sigma' = \frac{1}{F}\sigma_w S_w^n + \sigma'_s \tag{5}$$

The strongest polarization response is related to the presence of electrically conducting materials where charges polarize in the EDL as well as within electrical conductors, due to the so-called electrode polarization mechanism (Wong, 1979; Buecker et al., 2018). In the absence of electrical conductors, the strength of the polarization is lower than in the case of electrode polarization and is only related to the surface area and the surface charge of particles (Vinegar and Waxman, 1984; Leroy et al., 2008; Revil and Florsch, 2010; Buecker et al., 2019).

Landfills are typically characterized by a high electrical conductivity related to the increased salinity of leachate accumulating during the degradation of waste (Frid et al., 2017; Maurya et al., 2017). However, in the case of dry waste as well as CDW, the landfill can be related to a more resistive response than the surrounding materials which makes the delineation of the landfill body difficult (Leroux et al., 2007). Elevated electrical polarization can be observed in MSW landfills (Nguyen et al., 2018) mainly related to the presence of organic material (Aristodemou and Thomas-Betts, 2000; Leroux et al., 2007). Recently, Flores-Orozco et al. (2020) reported a linear relationship between electrical polarization and the total organic carbon (TOC) in MSW. Besides organic matter, the presence of metals in landfills cannot be neglected, as they lead to high polarization due to the electrode polarization mechanism (Aristodemou and Thomas-Betts, 2000; Bavusi et al., 2006).

IP measurements are sensitive to errors arising from polarization of the electrodes (when an electrode is used for voltage readings immediately after being used for current injection) as well as electromagnetic coupling related to cross-talk between the cables (Flores Orozco et al., 2021). To minimize the effect of cross-talk some studies have proposed the use of coaxial cables (e.g., Flores Orozco et al., 2021; Maierhofer et al., 2022); whereas others have proposed an alternative approach considering the separation of cables and electrodes used for current injection and potential measurements. Measurements with separated cables permit the use of multicore cables (Flores Orozco et al., 2021).

2.2 Modelling/inversion algorithm

For the forward modelling and the inversion of the data we used the ResIPy code (Blanchy et al., 2020; Boyd et al., 2019), which calls the cR3t 3D complex resistivity inversion code (for details in the algorithm, we refer to Binley and Slater, 2020). cR3t is finite element based, allowing discretization of the domain on a structured or unstructured mesh. To solve for the complex resistivity distribution in terms of the magnitude ($|\rho^*|$) and the phase (φ) the inversion algorithm iteratively aims to minimize an objective function, $\Psi(\mathbf{m})$, consisting of two terms (more details in Binley and Kemna, 2005):

$$\Psi(\mathbf{m}) = \Psi_d(\mathbf{m}) + \alpha\Psi_m(\mathbf{m}) \tag{6}$$

where $\mathbf{m}$ is the vector of model parameters (the logarithm of complex resistivities in cR3t), $\Psi_d(\mathbf{m})$ contains the difference between the given data ($\mathbf{d}$, the measured complex impedances) and the forward solution for parameter set $\mathbf{m}$, $\Psi_m(\mathbf{m})$ stabilizes the model objective function through regularization, weighted by parameter α, which controls the balance between the influence of the data misfit and the model objective function in the inversion (Binley and Kemna, 2005).

The total objective function is iteratively minimized by the Gauss-Newton method. At each iteration, the model is updated and α is determined by a line search. The iterative procedure continues until the model describes the data to a satisfactory level. cR3t uses a weighted least squares measure of data misfit (in $\Psi_d(\mathbf{m})$), which can be expressed as a root mean square misfit:

$$RMS = \sqrt{\frac{1}{n}\sum_{i=1}^{n}\frac{|d_i - F_i(\mathbf{m})|^2}{|\epsilon_i|^2}} \tag{7}$$

where d_i is measurement i, with associated measurement error ϵ_i and $F_i(\mathbf{m})$ is the computed measurement i for parameter set $\mathbf{m}$. The RMS is equal to one if the model describes the data satisfactorily (Binley and Slater, 2020). As a criterion for reliability of the complex conductivity inverse model we use the sensitivity (Jacobian) matrix $\mathbf{J}$ (for more details see: Binley and Slater, 2020). cR3t computes the complex resistivity model for a single frequency. Repeated inversion over multiple frequencies provides spectral information for each parameter cell, which can then be analyzed to determine relaxation model parameters for each cell. To fit Cole Cole parameters, we used the algorithm implemented by Ruecker et al. (2017) within the pyGIMLi libraries.

2.3 3D synthetic experiment and configurations

Single-frequency IP

To examine suitable electrode configurations for 3D single- and multi-frequency measurements, we conducted numerical modeling experiments, i.e., where the true electrical model is known. Thus, we can quantify the accuracy of our electrode configurations as a function of the difference between the true and inverted models. The single-frequency real model (see Fig. 1a) corresponds to an asymmetrically two-layered conductivity magnitude model with a pit-shape and a polarizable anomaly in the central area: the upper layer is resistive (10 mS/m) with a thickness of 3–5 m, depending on the direction, while the lower layer is a conductive area (50 mS/m). In the northern and western part, the upper layer has a depth of 3 m, while the depth in the southern and eastern part is 5 m. In the center of the model there is an 8 m deep low conductivity pit (10 mS/m). The width of the pit is 24 m on the bottom and 34 m on the top of the pit and the border of the pit has a slope of 45°. In the low conductivity pit, we embedded a cuboid IP anomaly with a conductivity phase of 30 mrad, while the surrounding areas have a background conductivity phase value of 5 mrad.

Multi-frequency IP

The multi-frequency synthetic model (see Fig. 1b) has the same geometry as the single-frequency model and consists of three regions with different Cole Cole models. Similar to the single-frequency model, regions 1 and 2 are resistive (10 mS/m), region 3 is conductive (50 mS/m). Region 1 is chargeable ($M = 0.4$) and the critical frequency is low ($f_{crit} = 0.5$ Hz), while in region 2 and 3 the chargeability is low ($M = 0.1$) and the critical frequency is high ($f_{crit} = 75$ Hz). The broadness of the spectra is equal for regions 1–3 ($c = 0.3$). The multi-frequency measurements were simulated in a frequency range of 0.1–240 Hz.

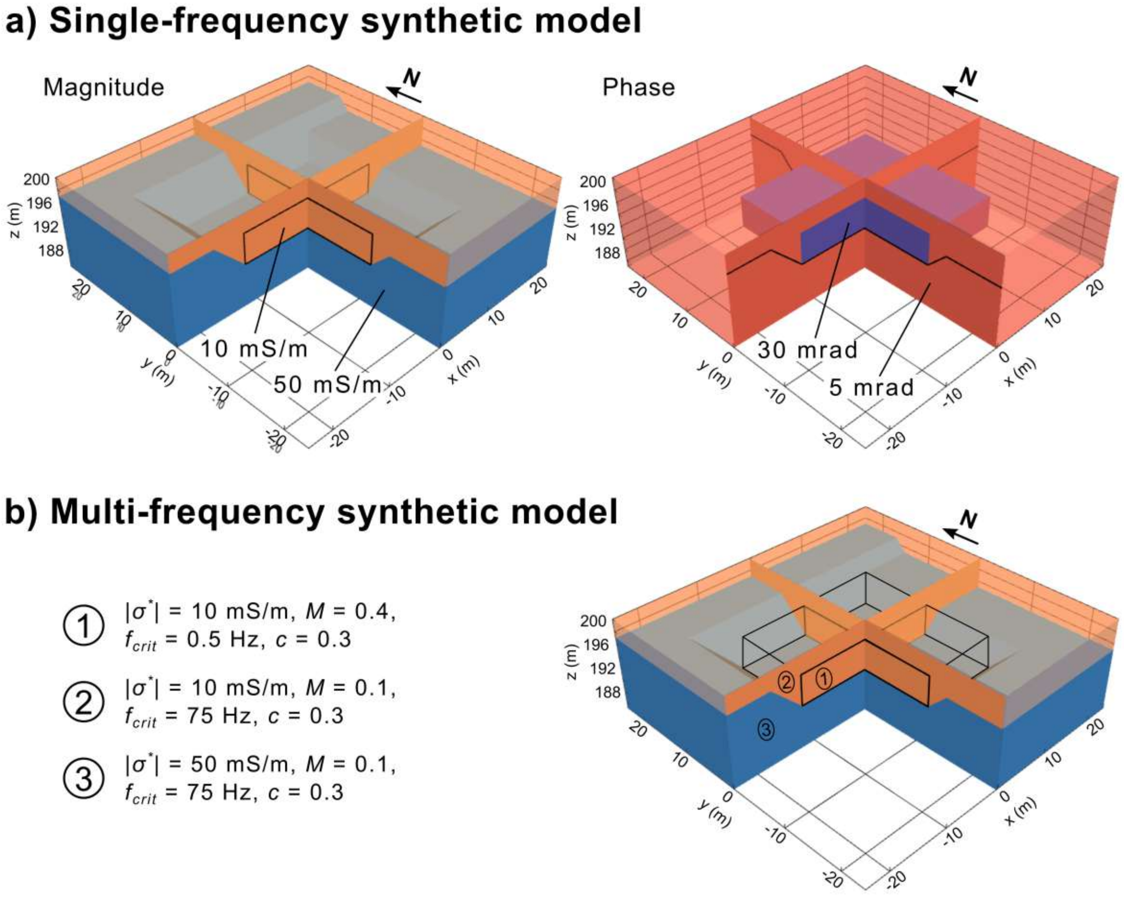

Fig. 1: Single-frequency (a) and multi-frequency (b) synthetic model. The single-frequency model is represented by the complex conductivity σ^* in terms of the magnitude $|\sigma^*|$ and the phase φ. The magnitude consists of a lower conductive layer (50 mS/m, blue) and an upper resistive layer (10 mS/m, orange), and a pit of the conductive layer in the center area. In the center of the single-frequency synthetic model there is a cuboid-shaped high-phase anomaly of 30 mrad (blue), surrounded by lower phase values of 5 mrad (red). Black lines indicate the boundary between the high and the low conductivity phase area (left) and the high and the low conductivity magnitude area (right). The multi-frequency-model has the same geometry and consists of three regions (1-3) with different Cole Cole models, which are given left to the synthetic model.

Configurations

Based on the described synthetic single-frequency subsurface model, we simulated FDIP measurements (magnitude and phase of the transfer impedance) of four different configurations with 64 electrodes per configuration (see Fig. 2). In configuration A we used single line measurements along two parallel straight lines with a separation of 20 m, 32 electrodes each and an electrode spacing of 2.5 m (see Fig. 2a). Configuration B is based on four parallel lines with a separation of 10 m between them, each line with 16 electrodes with a spacing of 5 m (see Fig. 2).

Configuration C and D represent true 3D measurements with more than one dipole direction. Configuration C is a grid array with 8 by 8 electrodes set in a rectangular grid with an electrode separation of 5 m in each direction. The electrodes are separated in two chains with 32 electrodes on each chain (see Fig. 2c). Configuration D is a circular array with electrodes set in four concentric circles with 7, 13, 19 and 24 electrodes, 5 m electrode separation within each circumference and circle radii of 5.575, 10.350, 15.125 and 19.100 m to keep a fair distribution of electrodes over the entire area of investigation (see Fig. 2d). The lines are set in a circular shape to increase the number of dipole orientations in the measurements, which is defined by the angle of a vector connecting both electrodes of a current or voltage dipole. Similar to configuration C line 1 and line 2 are physically separated lines, which are used to separate the current line from the potential line. We placed one electrode at the center of the circumferences (see Fig. 2d) to increase the sensitivity within that area. For the multi-frequency analysis, we simulated measurements with configurations B (representing 2D parallel lines) and C (representing true 3D measurements).

For the simulation of measurements, we used a dipole-dipole (DD) schedule, with a dipole length of once the electrode spacing (i.e., skip-0, using common notation). In the forward modeling we consider an error of 2% for the impedance magnitude and 1 mrad for the impedance phase for each configuration, while in the inversion we used a relative error of 2% and 2 mrad. We used a higher phase angle error in the inversion than in the forward modelling because when using an absolute phase error of 1 mrad in the inversion we observed slight overfitting in the results. Before inverting the simulated measurements, we removed quadrupoles with an infinite geometric factor (due to crossing voltage/current dipole direction in the center of the current/voltage dipole), as well as those forward measurements associated with a negative phase angle (as noted before, positive phase angles imply a capacitive effect).

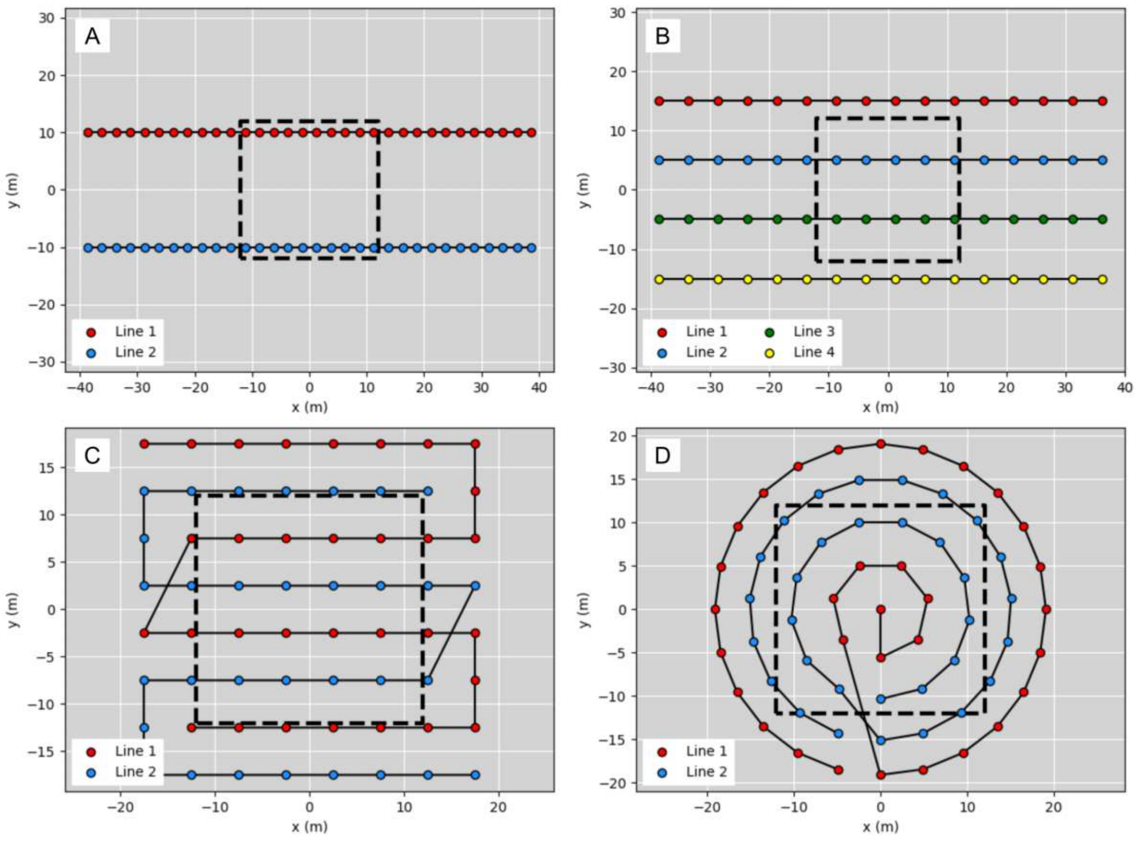

Fig. 2: Visualization of the electrode configurations which were used for the synthetic modeling. Configuration *A* and *B* consist of two/four parallel lines, while configuration *C* is represented by a grid of 8 by 8 electrodes connected by two separated lines, which are hairpin bended. Configuration *D* has four concentric lines with a line distance of 5 m approximately and an electrode separation of 5 m exactly. In the center of configuration *D* there is an additional single electrode to increase the resolution in the central area.

2.4 Field measurements

The field data were collected across two different landfills. In the Heferlbach landfill, we collected data in a shallow MSW area where extensive geophysical and ground truth data are available (Brandstätter et al., 2020; Flores-Orozco et al., 2020; Steiner et al., 2022). In the Kappern landfill we conducted measurements in a CDW area with a much thicker waste unit compared to the Heferlbach landfill.

2.4.1 Site 1 (landfill Heferlbach) - MSW and high polarization response

The landfill Heferlbach is located southeast of Vienna, Austria, in an oxbow lake of the river Danube (48° 8’ 50.3” N 16° 31’ 5.2” E) (see Fig. 3b). Between 1965 and 1974 the former riverbed was mainly filled with MSW, but also land excavation material and CDW with a total volume of 240000 m^3 (Austrian Environmental Agency, 2005). The 66000 m^2 large tube-shaped landfill is situated on an altitude of about 156–157 m asl (above sea level) with a mean waste depth between 3.0 and 4.5 m. Below the waste material there is an aquifer of quaternary gravels on top of a sand layer forming an aquiclude. The groundwater table is below the bottom of the waste area at 149 m asl approximately. Chemical analyses show a high rate of landfill gas production due to the high content of organic waste. To accelerate the degradation of organic materials and to avoid the migration of landfill gas into neighboring buildings a horizontal aeration pipes system was erected in 2012 (Brandstätter et al., 2020). We decided to conduct 3D SIP field measurements on an area with high content of MSW in the western-center part of the landfill (see Fig. 3b), where extensive information of the landfill is available (Flores-Orozco et al., 2020; Steiner et al., 2022). The host geological material (lower layer) can be characterized by a moderate conductivity ($\sim$ 30 mS/m), while the top layer is resistive ($<$ 10 mS/m). The highly conductive ($>$ 100 mS/m) and polarizing ($>$ 30 mrad) MSW unit has a thickness of 4 m approximately and is covered by a 0.5-1.0 m thick forest floor organic layer. More detailed information about the landfill can be found in Austrian Environmental Agency (2005), Brandstätter et al. (2020), Flores-Orozco et al. (2020) and Steiner et al. (2022).

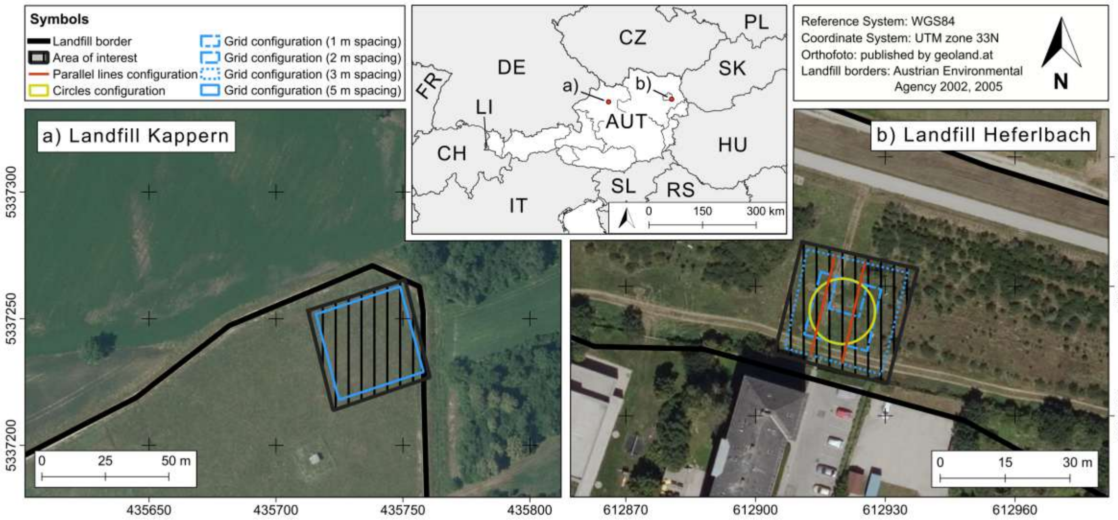

Fig. 3: Location of the study areas Kappern (a) and Heferlbach (b). The map upper center shows the locations of the landfills in relation to Central Europe. In the main maps the study areas of this paper are represented by a striped black rectangle. In Kappern measurements were conducted by using configuration C (grid array) with an electrode separation of 5 m (blue-colored rectangle). In Heferlbach measurements were conducted with configuration C and 1 m, 2 m and 3 m electrode separation (blue-colored rectangles). Moreover, configuration A consisting of two parallel lines (brown-colored lines) and configuration D consisting of 4 concentric lines (yellow-colored circle) were used.

2.4.2 Site 2 (landfill Kappern) - CDW and low polarization response

The landfill Kappern is located in Upper Austria, Austria, (48° 11' 4.0" N 14° 08' 4.8" E) (see Fig. 3a) on an altitude of 292.5 m asl in a former gravel pit, which was filled with MSW, CDW as well as industrial waste from 1974 to 1983 (Austrian Environmental Agency, 2002). The waste masses extend a volume of 120000 to 150000 m^3 on an area of 30000 m^2 and are on top of quaternary gravels of the nearby river Traun. The bottom of the landfill is in a depth of 3.5 to 5.5 m and was not proofed initially. Prior to 1998, leachate percolated into the groundwater body due to the high elevation of the groundwater table (288 m asl). Therefore, a sealing wall surrounding the main part of the landfill was built and the groundwater table was lowered below the landfill bottom, which prevented further potential groundwater pollution. To close the landfill on top the area was covered by multiple layers (about 2 m thick), including a layer of CDW, a gas drainage layer, a fleece, a geo textile, and a vegetated layer (Austrian Environmental Agency, 2002). Until now, there has been no studies examining possible landfill gas emissions, and, compared to the Heferlbach landfill, minimal chemical analysis studying the composition and distribution of waste.

2.4.3 SIP field measurements and data processing

In this study, we conducted field measurements with the DAS-M (Data Acquisition System Multisource, from MPT-IRIS Inc.), which permits the physical separation of the transmitter and the receiver: the transmitter is connected with a cable array to current electrodes and a second cable array connects the receiver and the voltage electrodes (see LaBrecque et al., 2021). The use of separated lines with physically independent transmitter and receiver with the DAS-M helps to decrease not only the effect of cross-talk between the cables but also within the instrument (Pelton et al., 1978; Dahlin et al., 2002b; Flores Orozco et al., 2021), thus, significantly increasing the quality of the IP data.

For all measurements, we used 5 m cables and hung them up on plastic tree protections to avoid loops with the cable and reduce sources of electromagnetic coupling. In the case of 2D lines, the separated cables were shifted by one electrode, according to the procedure of Dahlin et al. (2002). Each configuration consists of 64 electrodes (32 electrodes per line), we used DD measurements which provide the most flexible set of quadrupoles for 3D measurements (Chambers et al., 2002). For all field measurements, after injecting current in one line and measuring the potential in the other line, the current and potential lines were changed to provide a reciprocal measurement to each normal measurement (more details about normal-reciprocal pairs see in LaBrecque et al., 1996). At the Heferlbach landfill, we used configuration A (parallel lines), configuration C (grid array) with electrode separations of 1 m, 2 m and 3 m and configuration D (circular array) (see Tab. 1). At the landfill Kappern we used configuration C with two different skip sizes (i.e., dipole lengths) (see Tab. 1). All measurements were conducted in a frequency range of 1–240 Hz.

Site	Configuration	Electrode separation (m)	Lines separation (m)	Skips
Heferlbach	Parallel lines (A)	0.75	7	1, 3
	Grid array (C)	1	1	0
	Grid array (C)	2	2	0
	Grid array (C)	3	3	0, 3, 7
	Circular array (A)	2	2	0, 3
Kappern	Grid array (C)	5	5	0, 7

Tab. 1: Measurement details of the Heferlbach site and the Kappern site.

The field data were processed in three steps. (1) We calculated the geometric factors based on numerically modelled transfer resistances of a homogeneous subsurface and removed field measurements where the polarity is inconsistent with the simulated data. (2) The data were independently filtered for each frequency based on the statistical analysis of the relative and absolute normal reciprocal misfit (LaBrecque et al., 1996; Slater et al., 2000; Flores Orozco et al., 2012b). (3) In the case of multi-frequency analyses, quadrupoles, which were removed during the previous processing steps at least in one frequency, were removed in all frequencies to maintain the same quadrupoles for each frequency.

The inversions of all frequencies were started independently under consideration of a relative magnitude and an absolute phase error, which were estimated by the normal reciprocal misfit of the filtered data (e.g., Flores Orozco et al., 2012b). The relative magnitude error was 10%, while the absolute impedance phase error was 10 mrad for a frequency of 1 Hz (range of impedance phase shift data: 0-85 mrad). For higher frequencies we used the same relative magnitude error but the error for the impedance phase was up to 50 mrad in the case of 240 Hz (range of phase shift data: 20-200 mrad). All inversions resulted in an RMS value of about 1. For the inversion of the data, 3D unstructured tetrahedral meshes incorporating the local topography were built with Gmsh (Geuzaine and Remacle, 2009). Fine tetrahedron elements were created around the electrodes, with coarser elements with increasing distance from the electrode positions. The mesh was extended far beyond the survey area to account for 'infinite' current paths. All inversions presented are shown in terms of complex conductivity magnitude and phase angle. In the case of field results, mesh elements with a log_{10} sensitivity/max(sensitivity) $\leq$ -7.5 were blanked.

3 Results

3.1 Single-frequency synthetic results

Conductivity magnitude inversion results

The conductivity magnitude models for all configurations (as observed in Fig. 4) resolve similar structures: (i) a bottom layer with the highest values (25-50 mS/m), and (ii) a top layer with the lowest conductivity values (5-20 mS/m). The values for the two layers are in agreement with those defined in the synthetic model, with variations in the range of 18-43% for the top and bottom layer (see Tab. 2). Additionally, Fig. 4 reveals differences in the shape of the interface between the two layers.

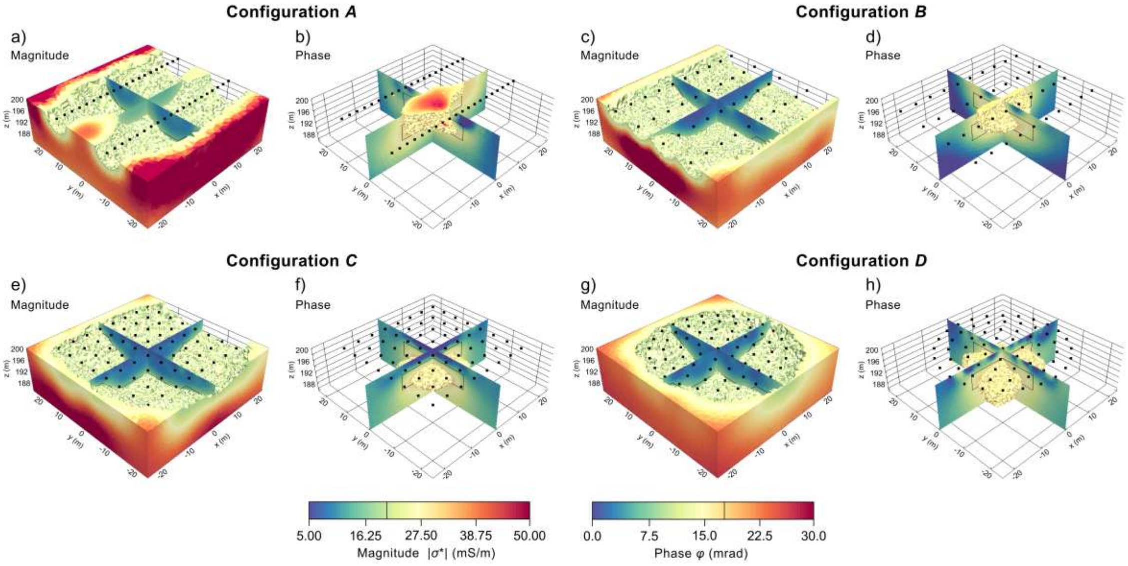

Fig. 4: Inversion results of simulated data of configuration *A*-*D*. For each configuration the results of the conductivity magnitude (a, c, e, g) and phase (b, d, f, h) are presented. Both parameters are visualized by two vertical slices, one parallel to the x-axis, one parallel to the y-axis. Additionally, all mesh elements with $|\sigma^*| > 20$ mS/m in the case of the magnitude and with $\varphi > 17.5$ mrad in the case of the phase are included. Black dots represent the electrodes positions.

Inversion results obtained for configuration *A* reveal that the interface between the top and bottom layers is correctly resolved below the electrodes (see Fig. 4a), yet the position of this interface is poorly resolved in the areas between the electrode lines resulting in the creation of artifacts, i.e., solving for a shallow interface. Configuration B represents a similar electrode geometry but with a shorter separation between the lines and a longer electrode spacing than in configuration A. Fig. 4c demonstrates that configuration B improves the imaging results and avoids the generation of artifacts in the conductivity magnitude images. However, both configurations A and B have only measurements collected along one direction, which leads to the creation of artifacts in the shape of ditches in the direction of the electrode lines (i.e., x-direction).

	NRMSE ($\lvert\sigma^*\rvert$) Top layer	NRMSE ($\lvert\sigma^*\rvert$) Bottom layer	NRMSE (φ) In anomaly	NRMSE (φ) Out of anomaly
Configuration A	42.80 %	36.78 %	58.28 %	69.46 %
Configuration B	23.00 %	37.97 %	58.43 %	48.68 %
Configuration C	18.60 %	37.80 %	61.10 %	23.60 %
Configuration D	22.48 %	42.79 %	50.48 %	40.92 %

Tab. 2: NRMSE in % between resolved conductivity magnitude and phase of inverse model and synthetic model.

Fig. 4e shows that configuration C is able to recover correctly the contact between the top and bottom layers. The recovered values in the top layer are more consistent with the true value (19% normalized root-median-square error (NRMSE)) than in the bottom layer (38% NRMSE). However, in the central uppermost area at a depth of < 1 m the inversion over-estimates the conductivity magnitude with maximum difference between true and inverse model of $> 50\%$.

As observed in Fig. 4g, the inversion of data using configuration D correctly solves for the geometry of the two layers, including the interface between them. However, the corners of the rectangular pit are poorly recovered, likely due to the lack of electrodes in the edges of the anomaly. The conductivity values are fairly well recovered for the two layers (22% and 43% NRMSE between inverse and real model for the top and bottom layer, respectively), but there are weak patterns of artifacts parallel to the circular electrode lines. Additionally, the shape of the interface between the top and bottom layer is not correctly resolved in the central area. Analysis of the sensitivity distribution (data not shown) reveal that the artifact observed in the center of Configuration D is related to the low sensitivity in this area.

Conductivity phase inversion results

In contrast to the magnitude results discussed above, there are large differences in the structures resolved in the phase imaging results for data collected with the different configurations tested. Inversion results for configuration A solved an IP anomaly in the center of the study area, but with a completely different shape compared to the IP anomaly in the true model (see Fig. 4b). Particularly, the upper boundary of the anomaly was not resolved by configuration A leading to the highest NRMSE value observed (69%) outside the anomaly. As observed in Fig. 4d, the resulting inverse model of configuration B is more consistent with the synthetic model than the inverse model of configuration A, not only regarding the values resolved for the conductivity magnitude top and bottom layer but also regarding the geometry of the conductivity phase anomaly and the absolute values in the anomaly (58% NRMSE).

The phase angle result for configuration C resolves for a similar geometry to that of the true model. The shape of the high phase anomaly is similar, but the depth of the lower interface between the area of high IP values and the background is not correctly resolved. Apart from the upper boundary, the position of the anomaly could be accurately determined in the x- and y-direction. The absolute values in the high phase anomaly are underestimated, compared to the values in the true model (61% NRMSE). Additionally, in near-surface areas (1–2 m depth) we can observe an over-shooting of the conductivity phase with values down to -5 mrad.

Such underestimation of values in the anomaly together with over-shooting outside of the anomaly is likely due to the use of a smoothing term in the regularization, as discussed by Binley and Slater, 2020).

The inversion results computed for configuration D reveal an accurate delineation of the position of the IP anomaly as well as in the recovered value. However, the geometry of the IP anomaly is poorly resolved, particularly the upper interface between the IP anomaly and the background in the center of the electrodes and the position of the lower interface; a loss of resolution at a depth of > 8 m is evident. Accordingly, configuration D is not able to correctly resolve the geometry of the anomaly.

3.2 Single-frequency field results for the MSW landfill Heferlbach collected with 3D different configurations and different electrode spacings

Raw data collected at 1 Hz in the Heferlbach landfill are presented as 3D pseudosections in Fig. 5 in terms of the resistance (R), the apparent resistivity (ρ_a) and the apparent phase shift (φ_a). The x- and y-direction assigned to each measurement correspond to the center position of the related current and potential dipole, while the pseudo depth of each measurement is inversely related to the distance between the current and potential dipoles. The pseudosections do not only give a first overview about the data quality but also permit a comparison of the range of the measured R, ρ_a and φ_a values between all configurations. In this regard, Fig. 5 reveals a similar range in the measured values (R, ρ_a and φ_a) for the three configurations tested here. The apparent resistivity values reveal a layered distribution, with the values of the second (central) layer being lower than those from the first (upper) and third (lower) layers. In contrast, the apparent phase shift values reveal higher values in the second layer (corresponding to the expected waste unit), with much lower values on the top and bottom layers.

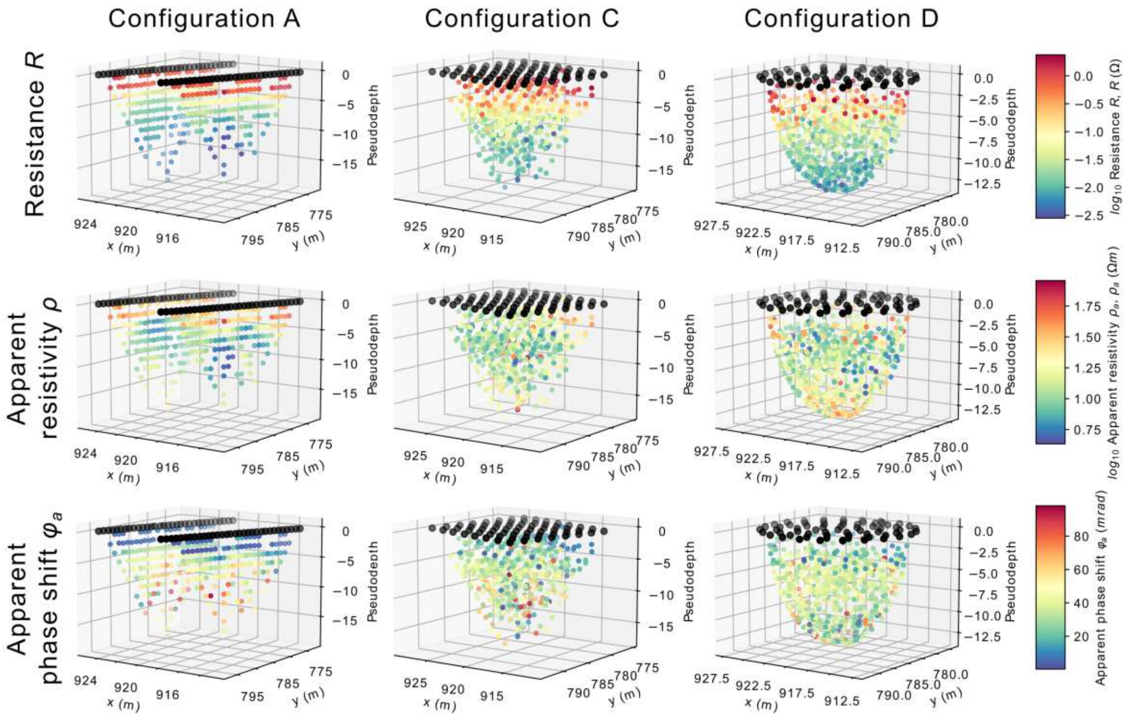

Fig. 5: 3D pseudosections of the Heferlbach data for configuration A, C and D at 1 Hz. Each measurement in terms of the resistance (R), the apparent resistivity (ρ_a) and the apparent phase shift (φ_a) is plotted on the mean position of the related current and potential electrodes, while the pseudo elevation of each measurement is inversely related to the distance between the current and potential dipoles. Black dots represent the electrodes positions.

The inverted results (in terms of conductivity magnitude and phase) at 1 Hz are presented in Fig. 6 as 2D horizontal slices corresponding to the resolved values at depths of 0.5, 1.5, 3.0 and 4.5 m for each configuration. In the inversion results of configuration A, we can observe a high conductivity magnitude and phase anomaly at a depth of 1 to 4 m along both lines and between the lines. In near surface areas (0.5 m) between both electrode lines, the conductivity magnitude and phase values differ dramatically from the values along the electrode lines due to a lack of sensitivity.

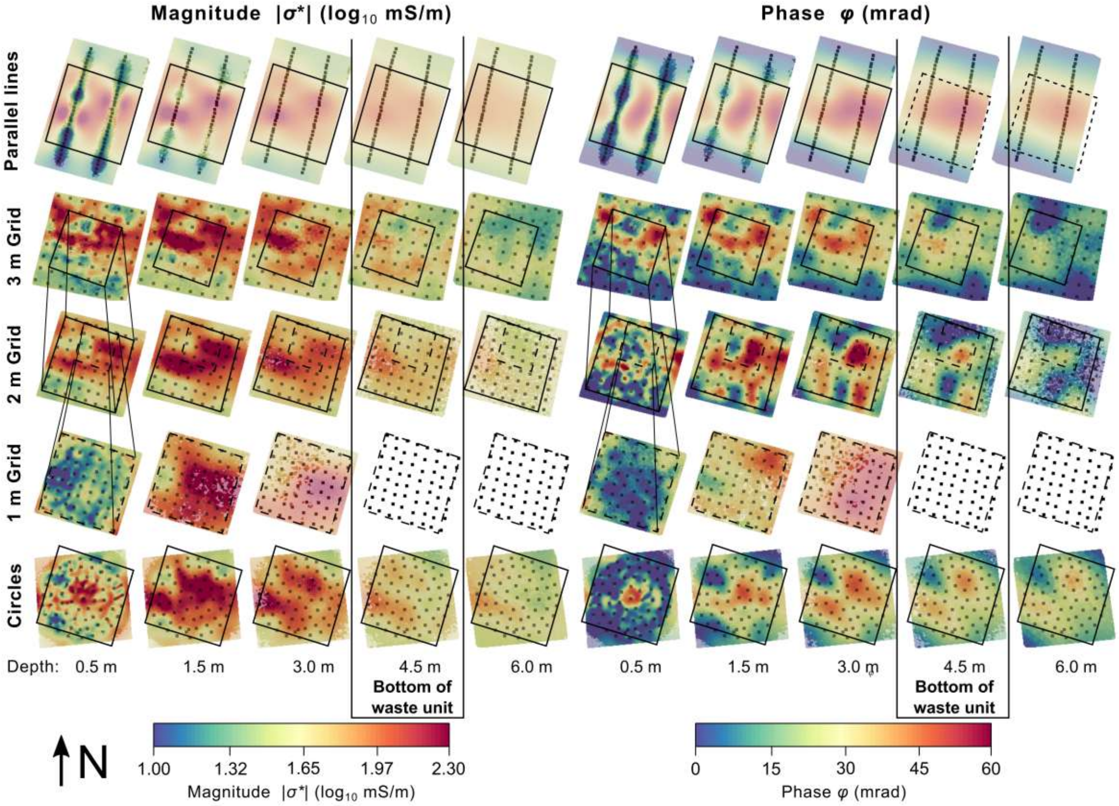

Fig. 6: Heferlbach inversion results of configuration A (line 1), C (line 2–4) and D (line 5) in terms of the magnitude (left) and the phase (right) of the complex conductivity at 1 Hz. For configuration C (line 2–4) the results of the configuration with 3 m, 2 m and 1 m electrode separation are presented. Mesh elements of low sensitivity ($\log_{10}$ sensitivity/max(sensitivity) $\leq$ -7.5) are transparently displayed. The bottom of the waste unit (according to Flores-Orozco et al., 2020) is displayed as two black vertical lines. The solid black rectangle represents the outline of configuration C with 2 m electrode separation, while the dashed black rectangle represents the outline of configuration C with 1 m electrode separation. Black dots represent the electrodes positions.

The results of configuration C collected with different electrode separations (3 m, 2 m and 1 m) presented in Fig. 6, reveal the effect of electrode spacing on the depths of investigation for the specific 3D configuration. As shown in Fig. 6, the main structures in the conductivity magnitude and phase are consistent for the 3D configuration with the different electrode spacing. As expected, deeper areas can be investigated by the 3 m electrode separation, which allows resolution of the lower boundary of the waste unit (at around 4.5 m depth, in agreement with sample analysis as presented by Flores-Orozco et al., 2020). However, for the 3 m electrode spacing, the upper boundary of the landfill is not resolved. In contrast, measurements with a 1 m electrode spacing resolve the contact of the waste unit with the top layer related to soil and CDW, as described by Flores-Orozco et al. (2020), yet these measurements are not able to determine the lower boundary of the waste because of a lack of sensitivity at depth. Accordingly, Fig. 6 reveals that only configuration C with an electrode separation of 2 m permits the delineation of both the lower and the upper boundary of the landfill. As a result, hereafter, in the case of configuration C, we will only discuss the results obtained with an electrode spacing of 2 m. The inverted data for configuration C delineate two anomalies characterized by the highest conductivity magnitude and phase values (> 100 mS/m and > 30 mrad, respectively). As discussed in detail by Flores-Orozco et al. (2020), these anomalies indicate biogeochemically active zones or hotspots, associated to the highest methanogenesis in the landfill.

The results of configuration D, presented in Fig. 6, show the delineation of both the upper and lower boundary of the waste unit. Even though the location of the two anomalies is similar to the results of configuration C, the shape of the anomaly is different. Such discrepancies are likely related to the lack of sensitivity in the center of configuration D as observed in the numerical modeling study. The lack of sensitivity also explains the discrepancies resolved between configuration C and D in the center of the investigation area.

In Fig. 7 we show the conductivity phase anomalies as volumes associated with values above 30 mrad, which correspond to the biogeochemical hot-spots and might be of particular interest due to their potential for high rates of methanogenesis (e.g., Flores-Orozco et al., 2020; Steiner et al., 2022). The position of the active zones extends to depths between 0.5 m and 4 m approximately and has a volume of 231 m^3 for configuration C and 309 m^3 for configuration D. We do not present such estimation for configuration A as Fig. 6 demonstrates that configuration A is only able to correctly solve the subsurface electrical properties directly below the electrode lines (2D) but not in the volume between the lines (3D).

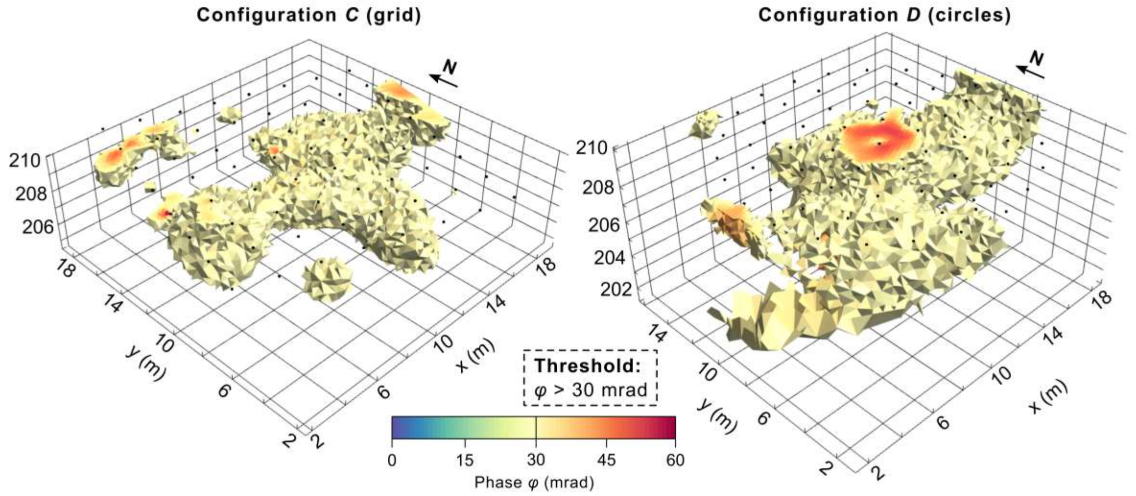

Fig. 7: Heferlbach 3D conductivity phase inversion results for configuration C (left) and D (right) at 1 Hz after removing all mesh elements with $\varphi < 30$ mrad. Black dots represent the electrodes positions.

3.3 Single-frequency field results for the CDW landfill Kappern

Building on the results discussed above, IP measurements in the Kappern landfill were only collected using configuration C with an electrode spacing of 5 m, resulting in the inverse models presented in Fig. 8. The inversions reveal an area of low conductivity magnitude ($\log_{10}|\sigma^*| < 0.9$ mS/m) in the center of the electrodes from the surface to a depth that varies between 4.5 and 8.5 m (or deeper). This anomaly is likely associated with CDW waste mainly consisting of coarse-grained materials such as concrete, bricks and other masonry material (Austrian Environmental Agency, 2002). Underneath the waste unit, the conductivity magnitude increases ($\log_{10}|\sigma^*| > 1.1$ mS/m), apart from a small area in the center-south and in the center-north, each at a distance of 7.5 m from the center of the electrodes. The increase of conductivity magnitude can be related to leachate migration (associated to high salinity and thus fluid conductivity) below the waste unit; however, it might also be indicative of a clay-rich unit corresponding to the low permeability layer underneath the landfill. No information from boreholes is known about the landfill for this area. In the waste unit, the conductivity phase values are low (< 5 mrad) and in agreement with the weak polarization of gravels and coarse materials (associated to low surface charge and area) at a frequency of 1 Hz. The layer below characterized by high φ values, might be indicative of a polarizable material, either due to organic materials leaking from the waste unit, or due to fine-grained material, which might show a polarization at low frequencies (see Flores Orozco et al., 2022; Zisser et al., 2010).

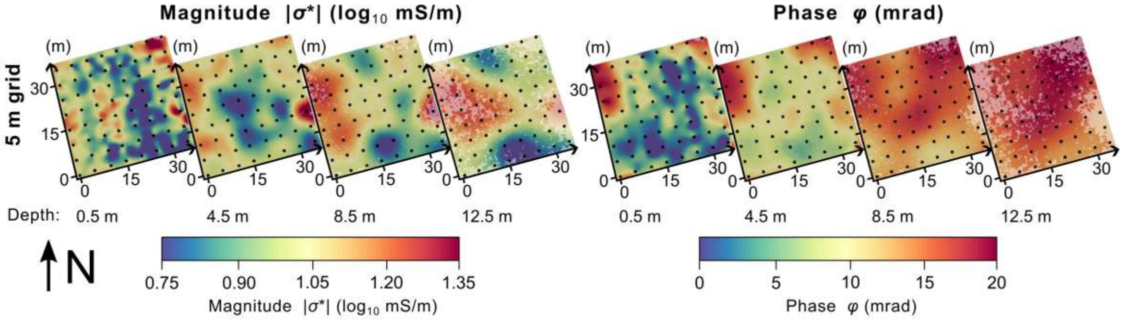

Fig. 8: Horizontal sections of the Kappern inversion results of configuration C in terms of the conductivity magnitude (left) and phase (right) at 1 Hz. Black dots represent the electrodes positions.

In Fig. 9 the conductivity magnitude and phase models are presented as 3D structures after removing all mesh elements with values above 0.9 $\log_{10}$ mS/m (in the case of the conductivity magnitude) and below 15 mrad (in the case of the conductivity phase) for a better impression about the shape of the above-described units. The high conductivity magnitude areas are related to the CDW waste unit with a volume of 3442 m^3, while the high conductivity phase areas correspond to a clay layer below the waste unit in a depth of about 8.5 m.

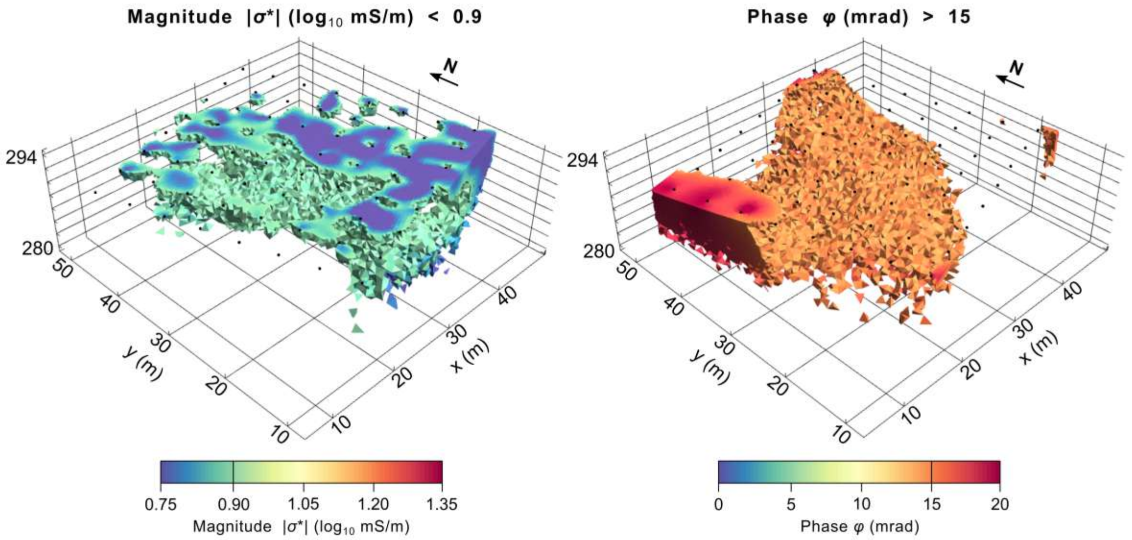

Fig. 9: Kappern 3D conductivity magnitude (left) and phase (right) inversion results for configuration C at 1 Hz after removing all mesh elements with $\log_{10}|\sigma^*| > 0.9$ (left) and $\varphi < 15$ mrad (right). Black dots represent the electrodes positions.

3.4 Multi-frequency (SIP) imaging results

In Fig. 10 we present the results of the conductivity phase angle for the frequencies 1, 15 and 75 Hz for configuration A and C in the landfill Heferlbach. Images of the conductivity magnitude reveal a minimal change for data collected at different frequencies and are in general similar to those presented in Fig. 6 and therefore not presented for the sake of brevity. Opposite to that, Fig. 10 reveals a significant frequency-dependence for the conductivity phase images, which can be further exploited to understand changes in waste composition, for instance. For both configurations A and C, the conductivity phase angle decreases from 1 to 15 Hz and increases from 15 to 75 Hz. Configuration C resolves for a consistent distribution of polarizable anomalies at different frequencies with a high resolution, while configuration A is not able to resolve the anomalies with the same level of detail, particularly for the areas between the electrode lines. The increase at 75 Hz is likely due to the polarization of the fine materials that migrate together with leachates and accumulated at the bottom of the landfill (e.g., Buecker et al., 2019). The polarization at low frequencies (e.g., 1 Hz and below) is most likely related to the presence of TOC, as also observed for measurements in peatlands with high TOC (Katona et al., 2021). As demonstrated by Flores-Orozco et al. (2020), the highly polarizable areas of the Heferlbach landfill are related to high concentration of organic waste and has been linked to TOC supporting our interpretation on the different polarization mechanisms underlying the response at 1 and 75 Hz. In this regard, 3D SIP might permit a better discrimination of polarizable anomalies due to biogeochemically active zones – associated to low frequencies – and fine-grained soil/waste with low TOC – related to a polarizable anomaly at high frequencies. Nonetheless, we point out here that the interpretation of the frequency-dependence of the imaging response is beyond the scope of this study and might be an open area of further research.

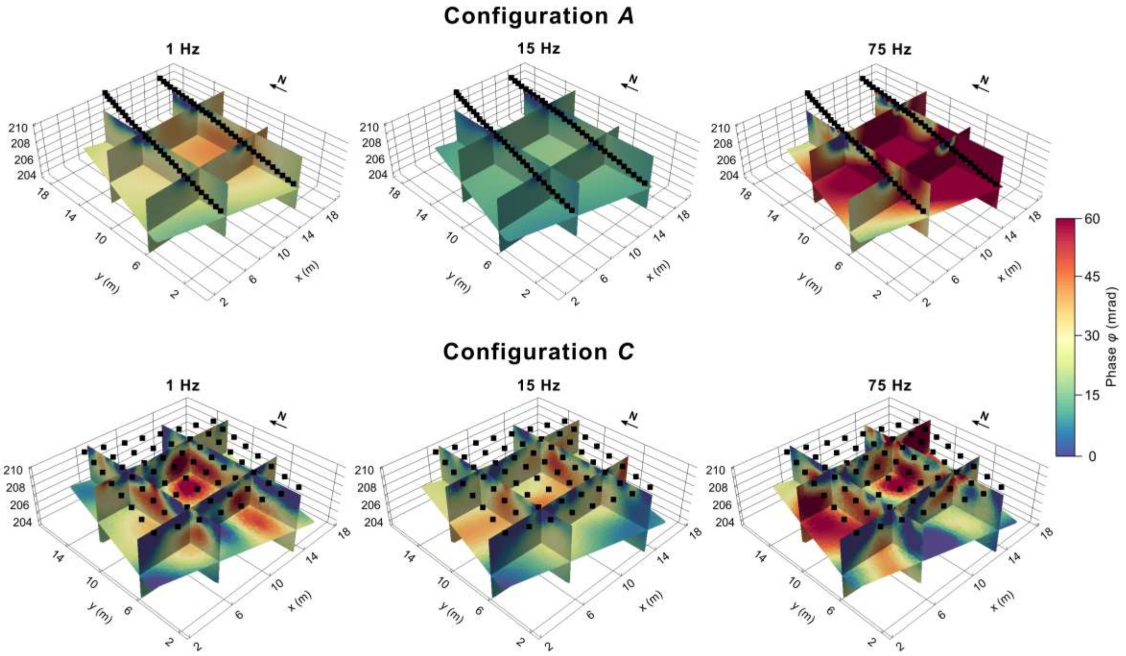

Fig. 10: Heferlbach conductivity phase angle inversion results for configuration *A* (first line) and *C* (second line) for frequencies 1, 15 and 75 Hz. Black dots represent the electrodes positions.

4 Discussion

4.1 2D versus 3D configurations in a simulated environment

The primary aim of this study was to test the resolving capabilities of four different electrode configurations (A to D) for 3D single- and multi-frequency IP investigations in landfills. Configurations A and B consist of parallel transects with inline measurements, while configurations C and D are true 3D IP electrode configurations with dipoles of different orientations. For each configuration, we simulated single-frequency IP measurements (conductivity magnitude and phase) on a cuboid-shaped high conductivity phase anomaly embedded in a low conductivity magnitude pit and tested the configuration for real IP measurements in two landfills. The inversion results demonstrate that the application of parallel collinear electrode arrays (configurations A and B) resolve the complex conductivity structures just in the area below the electrode lines, but these are not able to delineate accurately the subsurface electrical properties between the lines. In particular, the upper boundary of the IP anomaly was not detected leading to a wrong geometry of the IP anomaly. Such observations are in agreement with resistivity studies from Dahlin et al. (2002) and resistivity and IP studies from Chambers et al. (2002). Additionally, this study shows that the resolving capabilities of such 2D configurations are even poorer for IP than for the resistivity (59% NRMSE versus 35% NRMSE), which was also demonstrated qualitatively by Chambers et al. (2002).

In this study, we propose true 3D IP measurements with various dipole orientations. We tested a grid array (configuration C) consisting of 8x8 electrodes arranged in a rectangular pattern, and a circular array (configuration D) with four concentric circles with a constant electrode separation. Inversion results of synthetic measurement simulations demonstrate that both configurations are able to overcome the limitations of parallel collinear electrode arrays. Both configurations C and D resolved the transition between the (conductive) bottom layer and the (resistive) top layer not only close to the electrodes, but also in areas between the electrodes. Furthermore, the shape of the conductivity phase anomaly in the center of the synthetic model was resolved more accurately for configuration C and D than for configuration A and B. Based on our results, 3D configurations are critical for quantitative imaging, even in the case of relatively simple settings as those presented in our synthetic model. The use of several 2D lines even using 3D inversion algorithms may result in an incorrect quantification of the volumes related to the anomalies, as revealed in our numerical experiment (c.f., Fig. 4).

4.2 2D versus 3D configurations on the field

To investigate the potentials of the different configurations in real field conditions we tested configuration A, C and D on the Heferlbach MSW landfill. As in the synthetic modelling, the inversion of data collected along parallel 2D electrode lines (configuration A) is not able to resolve the upper and lower boundary of the waste unit (represented by high conductivity phase values) between the lines, due to a lack of sensitivity. The actual geometry, including the upper (depth $\approx$ 1 m) and lower (depth $\approx$ 4.5 m) boundary of the waste unit (see Flores-Orozco et al., 2020), was only resolved by data collected with configuration C with an electrode separation of 2 m in x- and y-direction. Using dipoles of different orientations, which were used in configuration C and D, allows resolution of heterogeneous subsurface electrical conditions, which, at this site, are likely to be the result of biogeochemically active zones in the landfill (Flores-Orozco et al., 2020). Such observation extends the conclusions of Chambers et al. (2002), who recommended to use not only one dipole orientation for heterogeneous subsurface electrical properties in 3D resistivity surveys, to IP measurements.

Furthermore, we tested the depth of investigation and the minimal resolution by applying three different electrode spacings (1, 2 and 3 m) for configuration C in the Heferlbach landfill. While a spacing of 2 m allows to solve the upper and lower boundary of the waste unit, an electrode separation of 3 m permits to solve the lower boundary but fails to solve the upper boundary; hence for 3 m spacing the depth of investigation is > 4.5 m and the minimal resolution is > 1 m. Decreasing the electrode separation to 1 m leads to the opposite result; hence the depth of investigation is < 4.5 m and the minimal resolution is < 1 m. Based on these observations we propose to use the following rules of thumb to roughly determine the depth of investigation and the minimal resolution of a 3D grid array: the depth of investigation corresponds to $1/3$ of the maximum separation between the current and voltage dipoles $dist_{dip}$ while the minimal resolution of the configuration can be estimated by $1/2$ of the electrode spacing $spac_{elec}$.

$$DOI = \frac{1}{3} max(dist_{dip}) \tag{8}$$

$$Resolution = \frac{1}{2} spac_{elec} \tag{9}$$

Further studies should consider the extension of the proposed experimental model in Equation 8 and 9 to include changes in the conductivity.

As an alternative to configuration C, we also tested four concentric circles (configuration D) on the Heferlbach landfill. While the inversion of these data is able to resolve the upper boundary of the high conductivity magnitude volume, the lower boundary of the high conductivity phase volume was not resolved. Moreover, the inversion of data collected with configuration D creates artifacts in the center of the electrodes. We observed similar artifacts in our numerical experiment. To improve the resolution in the central area of the concentric circles, we added more quadrupoles with an electrode in the center of the simulated data, which helped to reduce the creation of artifacts, i.e., results in a lower NRMSE value between resolved and true phase angle values in the IP anomaly (50% versus 60%). Alternatively, placing two electrodes used as a current or potential dipole in the center of the electrode array could improve the sensitivity.

Based on the synthetic modelling and the field results we recommend using configuration C for 3D IP surveys in landfill investigations because it provides a more accurate reconstruction of the shape of electrical anomalies in the subsurface. Moreover, building a grid of electrodes rather than circular arrays is easier to achieve in the field. Additionally, as discussed above, changing the size of configuration C provides clear advantages, as it permits to easily increase the resolution in near-surface areas, the actual extension of the explored area, or the total depth of investigation. Further investigations might also include the inversion of the three different meshes sizes (electrode separation of 1, 2 and 3 m) in a single dataset to quantify a possible improvement in the total area of coverage as well as in the resolution. A key message from this study is the need to perform numerical modeling sensitivity tests prior to carrying out field 3D IP surveys, to ensure optimal configuration of electrodes and measurements.

Due to the previously described advantages and disadvantages of the different 3D configurations, we decided to use configuration C on the Kappern CDW landfill. The inversion results show that the configuration is also able to delineate low conductivity magnitude anomalies related to CDW units and underlying high conductivity phase values, likely related to a lower clay layer.

4.3 Spectral IP (SIP) results of 2D and 3D synthetic data

Several studies have shown that collecting IP data at a broad frequency-bandwidth might provide further insights for an improved hydrogeological characterization (in comparison to single-frequency data), or to discriminate between different geochemical status (e.g., Flores Orozco et al., 2011). In particular, the frequency-dependence seems to be related to changes in the textural properties of the subsurface (see Binley et al., 2005; Revil and Florsch, 2010) and, thus, with the hydrogeological parameters (e.g., hydraulic conductivity). In this regard, it is important to understand the impact of 2D and 3D investigations in the quality of the resolved frequency-dependence of the complex conductivity.

As presented above, for single-frequency synthetic and field data, true 3D configurations provide more consistent complex conductivity results than 2D configurations. In Fig. 11 we expand such analysis to the frequency-dependence of the complex conductivity. We present the resulting spectra and the Cole Cole fit of the multi-frequency (0.1-240 Hz) inverse models for a 2D configuration (configuration B) and a 3D configuration (configuration C) (see Fig. 11a and b). We extract pixel values in two zones: (1) between electrode lines (referred to as $Z1$), and (2) directly below the electrodes (referred to as $Z2$) of configuration B (see Fig. 11d). Additionally, we estimated the relaxation parameters of the multi-frequency inverse models of $Z1$ and $Z2$ for configuration B and C and compare them with the true predefined relaxation parameters.

Fig. 11a and b demonstrate that configuration C provides more stable spectra (i.e., smoother) of both the conductivity magnitude (a) and phase (b) than configuration B as the spectra of configuration B are noisier than for Such observation is also shown by the lower NRMSE values between the resolved and corresponding Cole Cole fitted conductivity magnitude (Fig. 11c, i) and phase angle (Fig. 11c, ii) for configuration C than for configuration B. Moreover, in the case of configuration B

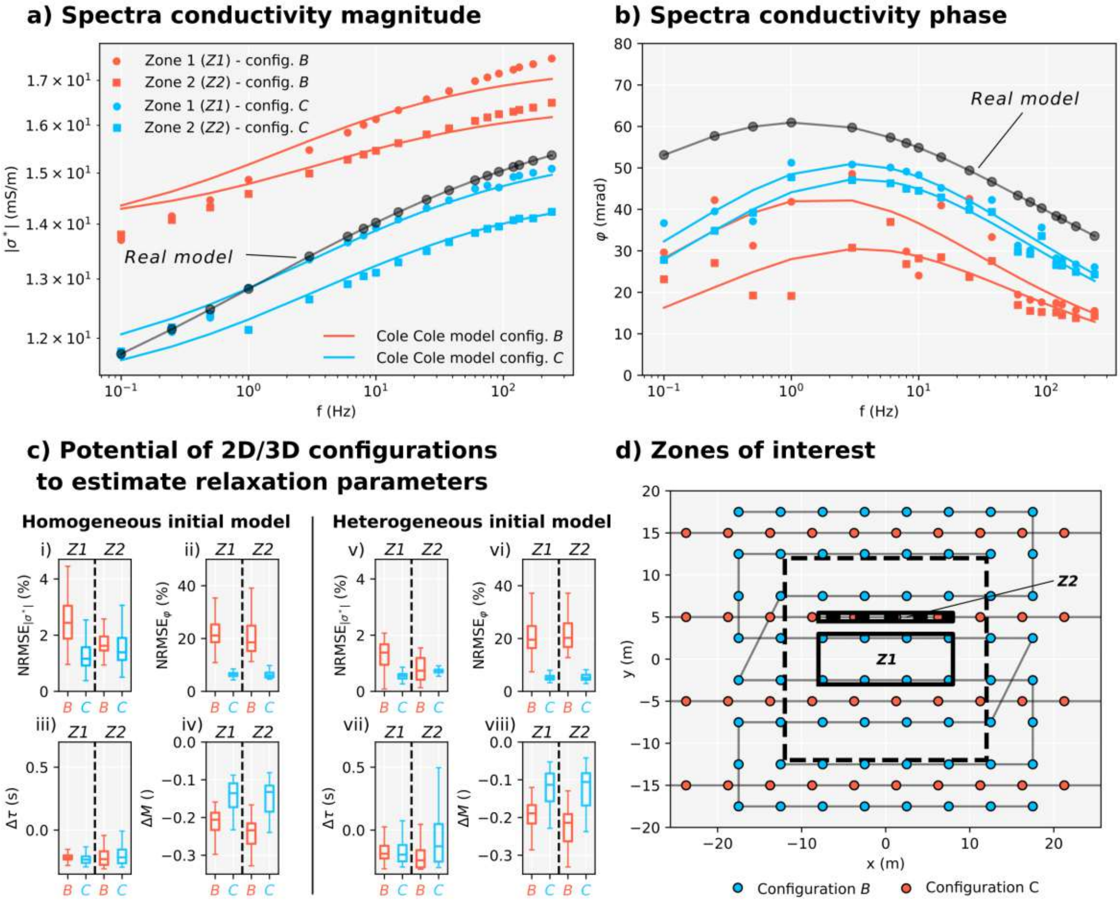

Fig. 11: Results of synthetic multi-frequency IP experiment of configuration B (red in entire Fig.) and C (blue in entire Fig.) in zone 1 ($Z1$, cuboid area in the center, $x = \pm 8$ m, $y = \pm 3$ m, $z = 193$–197 m) and zone 2 ($Z2$, cuboid area below electrodes of configuration B, $x = \pm 8$ m, $y = 4.5$–5.5 m, $z = 193$–197 m). The positions of $Z1$ and $Z2$ are presented in a map relative to the electrode positions (d). Subplots (a) and (b) present the spectra (frequency-range: 0.1-240 Hz) of the conductivity magnitude phase for pixels extracted in $Z1$ (circular shaped dots) and $Z2$ (square shaped dots) as well as the accompanying Cole Cole fits (solid lines). The true Cole Cole model is given by a black line. Subplots in (c) present the potential of configuration B and C to estimate relaxation parameters of the multi-frequency inverse models under the use of a homogeneous starting model (left) and a heterogeneous starting model (right). (i, ii, v, vi) represent the NRMSE between the extracted pixel values and the fitted Cole Cole model for the conductivity magnitude and phase, while subplots (iii, iv, vii, viii) present the absolute difference between true and estimated relaxation parameters τ and M.

the deviations are higher for areas between the electrode lines, where the single-frequency analysis demonstrated a vulnerability to the creation of artifacts. Thus, as observed in Fig. 11c, the resolved relaxation time τ (iii) and the chargeability M (iv) can be estimated more accurately with configuration C than with configuration

B with lower absolute differences between the estimated and the true relaxation parameters. The difference in the reconstruction quality between configuration B and C is lower for τ than for M. Such observation is in agreement with Weigand et al. (2017), who demonstrated that in 2D imaging the reconstruction quality of the chargeability is strongly related to the coverage while the reconstruction quality of τ is not dominated by the coverage. Thus, the application of 3D configurations over 2D configurations is particularly important for the estimation of the chargeability, which in turn could be very important for an adequate interpretation of waste composition (see Flores-Orozco et al., 2020) or the estimation of petrophysical parameters (see Steiner et al., 2022).

To improve the stability of the resolved frequency-dependence we inverted the simulated data for the resistivity of the lowest frequency and used the resulting resistivity model as initial model for the independent inversion of all frequencies. Subplots (v-viii) show that using the same heterogeneous initial model improves the recovered frequency-dependence of the inverse models, considering that such inversions provide lower NRMSE values between the resolved complex conductivity spectra and the spectra of fitted Cole Cole models for both configurations, particularly in the case of the conductivity magnitude (v). Further, the approach leads to a more accurate estimation of the relaxation parameters τ (vii) and M (viii) with median absolute deviations between estimated and true parameters closer to zero than in the case of a homogeneous initial model.

4.4 Spectral IP (SIP) results of 2D and 3D field data

Numerical experiments have demonstrated that 3D configurations provide less noisy spectra of the multi-frequency inverse models, in turn permitting a more accurate estimation of relaxation parameters than multi-frequency results of 2D configurations. For the case of field scale inversion results, estimating relaxation parameters is particularly challenging, considering that different sources of error might distort data collected at different frequencies, the unavoidable contamination of the data due to electromagnetic coupling, and the uncertainty associated with the inversion of the data across space and frequency. To consider the influence of such error sources in the frequency-dependence of SIP surveys, we present in Fig. 12 pixel values extracted from the multi-frequency inversion results (independently inverted) of the Heferlbach landfill, in terms of the magnitude and phase of the complex conductivity. The results are presented for configuration B and C for three positions of interest (see location in d) in the frequency range between 1 and 240 Hz.

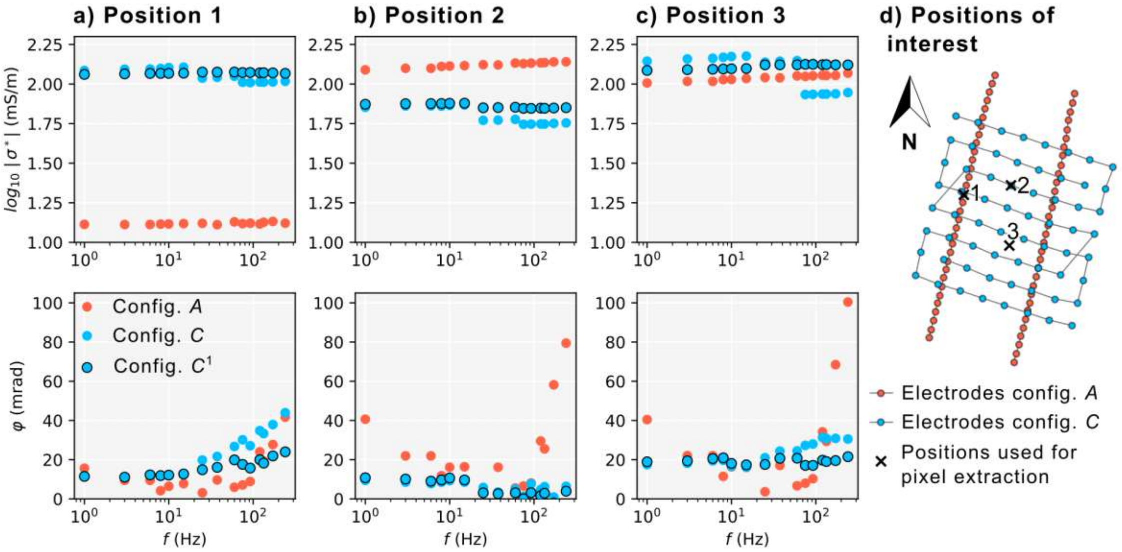

¹Using a heterogeneous initial model in the inversion.

Fig. 12: Conductivity magnitude (first row) and phase (second row) spectra (frequency range: 1-240 Hz) of the multi-frequency inversion result for three selected positions (a, b, c) (d: map representing the positions). Blue dots represent the results of configuration C, while red dots represent results of configuration A. Data of configuration C were also inverted using a heterogeneous initial model and are presented by blue dots with black edges.

Fig. 12 shows large differences of the conductivity magnitude and phase spectra between configuration A and C. While the magnitude spectra are smooth for both 2D and 3D configurations, distortions in the recovered frequency-dependence of the conductivity phase are evidenced, particularly for the 2D configuration. The mean discrete differences of the magnitude are lower for the 2D configuration (0.95 mS/m) than for the 3D configuration (3.53 mS/m) in all positions due to jumps in the magnitude of the 3D configuration. In contrast to the magnitude, the mean discrete differences of the phase angle are lower for configuration C (2.36 mrad) than for configuration B (9.56 mrad) in all positions. Moreover, for configuration A the spectrum in position 1 is less noisy than in position 2 and 3 revealing a lack of resolution in areas between the lines (position 2 and 3), which is in agreement with the single-frequency and synthetic multi-frequency results of 2D configurations.

The computation of consistent inversion results for multi-frequency SIP data sets is critical for quantitative imaging (see Flores Orozco et al., 2012; Weigand et al., 2017). However, independent inversions reveal noisy spectra as observed in Fig. 12. Following the same procedure as for the synthetic results, we ran a new set of independent inversions but using a heterogeneous initial model, which corresponds to the final inversion result for the data collected at the lowest frequency collected (0.5 Hz). We used the lowest frequency, as this represents the data set less affected by electromagnetic (EM) coupling (see Flores Orozco et al., 2021). Fig. 12 shows that using a heterogeneous initial model helps not only to reduce the dispersion of the conductivity magnitude spectra (0.69 mS/m versus 3.53 mS/m) but also stabilizes the conductivity phase spectra (1.81 mrad versus 2.36 mrad) in positions 1-3 of the inverse mesh.

As evidenced in Fig. 12 and the numerical experiment described above, the collection of data with real 3D configurations permits an improved reconstruction of the frequency dependence of the complex conductivity, in particular of the chargeability parameter. Hence, 3D configurations are critical on the field scale for the application of petrophysical models derived in the laboratory to quantify textural, hydrogeological or biogeochemical properties of the subsurface.

5 Conclusions

In this study we investigated the resolving capabilities of four different electrode configurations for 3D SIP surveys. In particular, we compared the capabilities of several parallel 2D profiles inverted within a 3D algorithm and real 3D configurations with dipoles varying within rectangular and circular grids. Our investigations were based on three steps: First, we numerically simulated single-frequency measurements for each configuration on a two-layered conductivity structure with an IP anomaly, inverted the data and compared them with the synthetic model. Second, we tested the configurations in a MSW and a CDW landfill. Third, we investigated the influence of 2D and 3D configurations on the frequency dependence by analyzing spectra of a multi-frequency synthetic and field survey.

The single-frequency synthetic inversion results demonstrate that while boundaries between two layers with different conductivity magnitudes could be delineated by all configurations, the geometry of the conductivity phase anomaly was not correctly resolved by all configurations. Configurations consisting of parallel 2D electrode lines with inline measurements were able to resolve the IP anomaly along the lines but failed to detect the anomaly between the lines due to a lack of sensitivity. In contrast, a 3D configuration with electrodes set in a quadratic mesh is able to resolve the geometry of the IP anomaly in the whole area of investigation; whereas a circular array with electrodes set in four concentric circles was not able to resolve the geometry of the IP anomaly as accurately.

The inversion results for field measurements conducted in two landfills confirms that parallel 2D arrays lack of sensitivity between the lines resulting in the creation of artifacts. Real 3D configurations were able to delineate the 3D geometry of IP anomalies, which are related to changes in landfill geometry and waste composition. However, the use of circular arrays reveals artifacts close to the surface. The use of electrodes placed on a 3D rectangular mesh also permits to easily change electrode spacing to gain information about different area and depth of investigation. Measurements of dipoles in a 3D rectangular mesh with an electrode spacing of 1 and 3 m in the Heferlbach landfill allowed to introduce rules of thumb for the depth of investigation (1/3 of the maximum separation between the current and voltage dipoles) and the minimal resolution (1/2 of the electrode spacing) for 3D grid arrays.

Our multi-frequency numerical and field measurements demonstrated that 3D configurations provide more stable spectra of the complex conductivity than 2D configurations. Spectra of 2D configurations are particularly noisy in areas between the electrode lines, where single-frequency results revealed a high vulnerability to artifacts. Thus, relaxation parameters describing the frequency-dependence of the complex conductivity can be estimated more accurately by 3D configurations.

References

Abdulsamad, F., A. Revil, A. Soueid Ahmed, A. Coperey, M. Karaoulis, S. Nicaise, and L. Peyras, 2019, Induced polarization tomography applied to the detection and the monitoring of leaks in embankments: Engineering Geology, 254, 89–101.

Aizebeokhai, A. P., and V. S. Singh, 2013, Field evaluation of 3D geo-electrical resistivity imaging for environmental and engineering studies using parallel 2D profiles: Current Science, 105, no. 4, 504–512.

Austrian Environmental Agency, 2002, Altlast O13 „Deponie Kappern". Beschreibung der Sicherungsmaßnahmen. Online (10.01.2023): https://www.altlasten.gv.at/atlas/verzeichnis/Oberoesterreich/Oberoesterreich-O13.html

Austrian Environmental Agency, 2005, Altablagerung „Heferlbach". Gefährdungsabschätzung und Prioritätenklassifizierung. (§13 und §14 Altlastensanierungsgesetz). Online (10.01.2023): https://www.altlasten.gv.at/atlas/verzeichnis/Niederoesterreich/Niederoesterreich-N58.html

Archie, G. E., 1942, The electrical resistivity log as an aid in determining some reservoir characteristics: Transactions of the American Institute of Mining and Metallurgical Engineers, 146, 54–62.

Argote-Espino, D., A. Tejero-Andrade, G. Cifuentes-Nava, L. Iriarte, S. Farías, R. E. Chávez, and F. López, 2013, 3D electrical prospection in the archaeological site of El Pahñú, Hidalgo State, Central Mexico: Journal of Archaeological Science, 40, 1213–1223.

Aristodemou, E., and A. Thomas-Betts, 2000, DC resistivity and induced polarisation investigations at a waste disposal site and its environments: Journal of Applied Geophysics, 44, 275–302.

Atekwana, E. A., and E. A. Atekwana, 2010, Geophysical Signatures of Microbial Activity at Hydrocarbon Contaminated Sites: A Review: Surveys in Geophysics, 31, 247–283.

Auken, E., J. Doetsch, G. Fiandaca, A. V. Christiansen, A. Gazoty, A. G. Cahill, and R. Jakobsen, 2014, Imaging subsurface migration of dissolved CO2 in a shallow aquifer using 3-D time-lapse electrical resistivity tomography: Journal of Applied Geophysics, 101, 31–41.

Bavusi, M., E. Rizzo, and V. Lapenna, 2006, Electromagnetic methods to characterize the Savoia di Lucania waste dump (Southern Italy): Environmental Geology, 51, 301–308.

Bentley, L. R., and M. Gharibi, 2004, Two- and three-dimensional electrical resistivity imaging at a heterogeneous remediation site: Geophysics, 69, no. 3, 674–680.

Bichet, V., E. Grisey, and L. Aleya, 2016, Spatial characterization of leachate plume using electrical resistivity tomography in a landfill composed of old and new cells (Belfort, France): Engineering Geology, 211, 61–73.

Bièvre, G., L. Oxarango, T. Günther, D. Goutaland, and M. Massardi, 2018, Improvement of 2D ERT measurements conducted along a small earth-filled dyke using 3D topographic data and 3D computation of geometric factors: Journal of Applied Geophysics, 153, 100–112.

Binley, A., and A. Kemna, 2005, DC resistivity and induced polarization methods, in Y. Rubin, and S. S. Hubbard, eds., Hydrogeophysics: Springer, 129–156.

Binley, A., L. D. Slater, M. Fukes, and G. Cassiani, 2005, Relationship between spectral induced polarization and hydraulic properties of saturated and unsaturated sandstone: Water Resources Research, 41.

Binley, A., and L. Slater, 2020, Resistivity and induced polarization: Theory and Applications to the Near-Surface Earth: Cambridge University Press.

Blanchy, G., Saneiyan S., Boyd J., McLachlan P., and Binley A., 2020, ResIPy, an intuitive open source software for complex geoelectrical inversion/modeling: Computers & Geosciences, 137.

Bording, T. S., G. Fiandaca, P. K. Maurya, E. Auken, A. V. Christiansen, N. Tuxen, K. E. S. Klint, and T. H. Larsen, 2019, Cross-borehole tomography with full-decay spectral time-domain induced polarization for mapping of potential contaminant flow-paths: Journal of Contaminant Hydrology, 226.

Boyd, J., G. Blanchy, S. Saneiyan, P. McLachlan, A. Binley, 2019, 3D Geoelectrical Problems With ResiPy, an Open Source Graphical User Interface for Geoelectrical Data Processing: Fast Times, 24, 85–92.

Boyd, J., J. Chambers, P. Wilkinson, M. Peppa, A. Watlet, M. Kirkham, L. Jones, R. Swift, P. Meldrum, S. Uhlemann, and A. Binley, 2021, A linked geomorphological and geophysical modelling methodology applied to an active landslide: Landslides.

Brandstätter, C., R. Prantl, and J. Fellner, 2020, Performance assessment of landfill in-situ aeration – A case study: Waste Management, 101, 231–240.

Brunner, I., S. Friedel, F. Jacobs, and E. Danckwardt, 1999, Investigation of a Tertiary maar structure using three-dimensional resistivity imaging: Geophysical Journal International, 136, 771–780.

Buecker, M., A. Flores Orozco, and A. Kemna, 2018, Electrochemical polarization around metallic particles — Part 1: The role of diffuse-layer and volume-diffusion relaxation: Geophysics, 83, no. 4, E203–E217.

Buecker, M., A. Flores Orozco, S. Undorf, and A. Kemna, 2019, On the role of Stern- and diffuse-layer polarization mechanisms in porous media: Journal of Geophysical Research: Solid Earth, 124.

Cassiani, G., A. Kemna, A. Villa, and E. Zimmermann, 2009, Spectral induced polarization for the characterization of free-phase hydrocarbon contamination of sediments with low clay content: Near Surface Geophysics, 7, 547–562.

Chambers, J. E., R. D. Ogilvy, O. Kuras, J. C. Cripps, and P. I. Meldrum, 2002, 3D electrical imaging of known targets at a controlled environmental test site: Environmental Geology, 41, 690–704.

Chambers, J. E., O. Kuras, P. I. Meldrum, R. D. Ogilvy, and J. Hollands, 2006, Electrical resistivity tomography applied to geologic, hydrogeologic, and engineering investigations at a former waste-disposal site: Geophysics, 71, no. 6, B231–B239.

Chambers, J. E., P. B. Wilkinson, A. L. Weller, P. I. Meldrum, R. D. Ogilvy, and S. Caunt, 2007, Mineshaft imaging using surface and crosshole 3D electrical resistivity tomography: A case history from the East Pennine Coalfield, UK: Journal of Applied Geophysics, 62, 324–337.

Chambers, J. E., P. B. Wilkinson, D. Wardrop, A. Hameed, I. Hill, C. Jeffrey, M. H. Loke, P. I. Meldrum, O. Kuras, M. Cave, and D. A. Gunn, 2012, Bedrock detection beneath river terrace deposits using three-dimensional electrical resistivity tomography: Geomorphology, 177–178, 17–25.

Chenq, Q., X. Chen, M. Tao, and A. Binley, 2019, Characterization of Karst Structures using Quasi-3D Electrical Resistivity Tomography: Environmental Earth Sciences, 78(15).

Christophersen, M., and P. Kjeldsen, 2001, Lateral gas transport in soil adjacent to an old landfill: factors governing gas migration: Waste Management and Research, 19, 144–159.

Clément, R., M. Descloitres, T. Günther, L. Oxarango, C. Morra, J.-P. Laurent, and J.-P. Gourc, 2010, Improvement of electrical resistivity tomography for leachate injection monitoring: Waste Management, 30, 452–464.

Dahlin, T., and C. Bernstone, 1997, A Roll-Along Technique For 3D Resistivity Data Acquisition With Multi-Electrode Arrays: Proceedings SAGEEP'97, Reno, Nevada, 2, 927–935.

Dahlin, T., C. Bernstone, and M. H. Loke, 2002a, A 3-D resistivity investigation of a contaminated site at Lernacken, Sweden: Geophysics, 67, no. 6, 1692–1700.

Dahlin, T., V. Leroux, and J. Nissen, 2002b, Measuring techniques in induced polarisation imaging: Journal of Applied Geophysics, 50, 279–298.

Dahlin, T., H. Rosqvist, and V. Leroux, 2010, Resistivity-IP mapping for landfill applications: Near Surface Geophysics, first break 28, no. 8, 101–105.

De Carlo, L., M. T. Perri, M. C. Caputo, R. Deiana, M. Vurro, and G. Cassiani, 2013, Characterization of a dismissed landfill via electrical resistivity tomography and mise-à-la-masse method: Journal of Applied Geophysics, 98, 1–10.

Di Maio, R., S. Fais, P. Ligas, E. Piegari, R. Raga, and R. Cossu, 2018, 3D geophysical imaging for site-specific characterization plan of an old landfill: Waste Management, 76, 629–642.

Flores Orozco, A., K. H. Williams, P. E. Long, S. S. Hubbard, and A. Kemna, 2011, Using complex resistivity imaging to infer biogeochemical processes associated with bioremediation of an uranium-contaminated aquifer: Journal of Geophysical Research, 116.

Flores Orozco, A., A. Kemna, C. Oberdörster, L. Zschornack, C. Leven, P. Dietrich, and H. Weiss, 2012a, Delineation of subsurface hydrocarbon contamination at a former hydrogenation plant using spectral induced polarization imaging: Journal of Contaminant Hydrology, 136–137, 131–144.

Flores Orozco, A., A. Kemna, and E. Zimmermann, 2012b, Data error quantification in spectral induced polarization imaging: Geophysics, 77, no. 3, E227–E237.

Flores-Orozco, A., J. Gallistl, M. Steiner, C. Brandstätter, and J. Fellner, 2020, Mapping biogeochemically active zones in landfills with induced polarization imaging: The Heferlbach landfill: Waste Management, 107, 121–132.

Flores Orozco, A., L. Aigner, J. Gallistl, 2021, Investigation of cable effects in spectral induced polarization imaging at the field scale using multicore and coaxial cables: Geophysics, 86, 1, E5–E57.

Flores Orozco, A., M. Steiner, T. Katona, N. Roser, C. Moser, M. J. Stumvoll, and T. Glade, 2022, Application of induced polarization imaging across different scales to understand surface and groundwater flow at the Hofermuehle landslide: Catena, 219.

Frid, V., I. Sharabi, M. Frid, and A. Averbakh, 2017, Leachate detection via statistical analysis of electrical resistivity and induced polarization data at a waste disposal site (Northern Israel): Environmental Earth Sciences, 76, no. 233.

Gallistl, J., D. Schwindt, B. Jochum, L. Aigner, M. Peresson, and A. Flores Orozco, 2022, Quantification of soil textural and hydraulic properties in a complex conductivity imaging framework: Results from the Wolfsegg slope: Frontiers in Earth Science, 10.

Gazoty, A., G. Fiandaca, J. Pedersen, E. Auken, and A.V. Christiansen, 2012, Mapping of landfills using time-domain spectral induced polarization data: the Eskelund case study: Near Surface Geophysics, 10, 575–586.

Geuzaine, C., and J.-F. Remacle, 2009, Gmsh: A 3-D finite element mesh generator with built-in pre- and post-processing facilities: International Journal for Numerical Methods in Engineering, 79, 1309–1331.

Han, Z., H. Ma, G. Shi, L. He, L. Wei, and Q. Shi, 2016, A review of groundwater contamination near municipal solid waste landfill sites in China: Science of the Total Environment, 569–570, 1255–1264.

Iliceto, V., and G. Morelli, 1999, Environmental assessment of municipal waste dump sites with electrical resistivity and induced polarization multielectrode methods, in Proceedings of the 5th meeting of the EEGS (Environmental and Engineering Geophysics Society)– European Section, Budapest, Hungary, September 6–9. EEGS, the Environmental and Engineering Geophysical Society, European Section, Lausanne, Switzerland.

Johansson, B., S. Jones, T. Dahlin, and P. Flyhammar, 2007, Comparisons of 2D and 3D Inverted Resistivity Data As Well As of Resistivity and IP Surveys on a Landfill: Proceedings of the 13th Near Surface Geophysics Conference, EAGE, Istanbul, Turkey, 3–5 September, P42.

Johnson, T. C., R. J. Versteeg, A. Ward, F. D. Day-Lewis, and A. Revil, 2010, Improved hydrogeophysical characterization and monitoring through parallel modeling and inversion of time-domain resistivity and induced-polarization data: Geophysics, 75, no. 4, WA27–WA41.

Johnson, T., R. Versteeg, J. Thomle, G. Hammond, X. Chen, and J. Zachara, 2015, Four-dimensional electrical conductivity monitoring of stage-driven river water intrusion: Accounting for water table effects using a transient mesh boundary and conditional inversion constraints: Water Resources Research, 51, 6177–6196.

Katona, T., B. S. Gilfedder, S. Frei, M. Buecker, and A. Flores-Orozco, 2021, High-resolution induced polarization imaging of biogeochemical carbon turnover hotspots in a peatland: Biogeosciences, 18, 4039–4058.

Kemna, A., A. Binley, G. Cassiani, E. Niederleithinger, A. Revil, L. Slater, K. H. Williams, A. Flores Orozco, F.-H. Haegel, A. Hördt, S. Kruschwitz, V. Leroux, K. Titov, and E. Zimmermann, 2012, An overview of the spectral induced polarization method for near-surface applications: Near Surface Geophysics, 10, 453–468.

LaBrecque, D., M. Miletto, W. Daily, A. Ramirez, and E. Owen, 1996, The effect of noise on Occam's inversion of resistivity tomography data: Geophysics, 61, no. 2, 538–548.

LaBrecque, D., R. Birken, D. LaBrecque, 2021, Design of a Multi-Source Capable, Hybrid Cabled/Distributed ERT/IP Data Acquisition System: SEG Technical Program Expanded Abstracts, 3063–3067.

Leroux, V., T. Dahlin, and M. Svensson, 2007, Dense resistivity and induced polarization profiling for a landfill restoration project at Härlöv, Southern Sweden: Waste Management and Research, 25, 49–60.

Leroy, P., A. Revil, A. Kemna, P. Cosenza, and A. Ghorbani, 2008, Complex conductivity of water-saturated packs of glass beads: Journal of Colloid and Interface Science, 321, 103–117.

Loke, M. H., and R. D. Barker, 1996, Practical techniques for 3D resistivity surveys and data inversion: Geophysical Prospecting, 44, 499–523.

Lou, X. F., and J. Nair, 2009, The impact of landfilling and composting on greenhouse gas emissions – A review: Bioresource Technology, 100, 3792–3798.

Maierhofer, T., C. Hauck, C. Hilbich, A. Kemna, and A. Flores-Orozco, 2022, Spectral induced polarization imaging to investigate an ice-rich mountain permafrost site in Switzerland: The Cryosphere, 16.

Maurya, P. K., V. K. Rønde, G. Fiandaca, N. Balbarini, E. Auken, P. L. Bjerg, and A. V. Christiansen, 2017, Detailed landfill leachate plume mapping using 2D and 3D electrical resistivity tomography - with correlation to ionic strength measured in screens: Journal of Applied Geophysics, 138, 1–8.

McAnallen, L., R. Doherty, S. Donohue, P. Kirmizakis, and C. Mendonça, 2018, Combined use of geophysical and geochemical methods to assess areas of active, degrading and restored blanket bog: Science of The Total Environment, 621, 762–771.

Nguyen, F., R. Ghose, I. Isunza Manrique, T. Robert, and G. Dumont, 2018, Managing past landfills for future site development: A review of the contribution of geophysical methods: Paper read at Proceedings of the 4th International Symposium on Enhanced Landfill Mining.

Nimmer, R. E., J. L. Osiensky, A. M. Binley, and B. C. Williams, 2008, Three-dimensional effects causing artifacts in two-dimensional, cross-borehole, electrical imaging: Journal of Hydrology, 359, 59–70.

Nordsiek, S., and A. Weller, 2008, A new approach to fitting induced-polarization spectra: Geophysics, 73, no. 6, F235–F245.

Nyquist, J. E., and M. J. S. Roth, 2005, Improved 3D pole-dipole resistivity surveys using radial measurement pairs: Geophysical Research Letters, 32.

Pelton, W. H., S. H. Ward, P. G. Hallof, W. R. Sill, and P. H. Nelson, 1978, Mineral discrimination and removal of inductive coupling with multifrequency IP: Geophysics, 43, no. 3, 588–609.

Revil, A., A. Coperey, Z. Shao, N. Florsch, I. L. Fabricius, Y. Deng, J. R. Delsman, P. S. Pauw, M. Karaoulis, P. G. B. de Louw, E. S. van Baaren, W. Dabekaussen, A. Menkovic, and J. L. Gunnink, 2017, Complex conductivity of soils: Water Resources Research, 53, 7121–7147.

Revil, A., A. Soueid Ahmed, A. Coperey, L. Ravanel, R. Sharma, and N. Panwar, 2020, Induced polarization as a tool to characterize shallow landslides: Journal of Hydrology, 589.

Revil, A., and N. Florsch, 2010, Determination of permeability from spectral induced polarization in granular media: Geophysical Journal International, 181, 1480–1498.

Revil, A., M. Schmutz, F. Abdulsamad, A. Balde, C. Beck, A. Ghorbani, and S. S. Hubbard, 2021, Field-scale estimation of soil properties from spectral induced polarization tomography: Geoderma, 403.

Ruecker, C., T. Guenther, and F. M. Wagner, 2017, pyGIMLi: An open-source library for modelling and inversion in geophysics: Computers and Geosciences, 109, 106–123.

Schurr, J. M., 1964, On the theory of the dielectric dispersion of spherical colloidal particles in electrolyte solution: The Journal of Physical Chemistry, 68, 2407–2413.

Slater, L., A. M. Binley, W. Daily, and R. Johnson, 2000, Cross-hole electrical imaging of a controlled saline tracer injection: Journal of Applied Geophysics 44, 85–102.

Slater, L., D. Ntarlagiannis, Y. R. Personna, and S. Hubbard, 2007, Pore-scale spectral induced polarization signatures associated with FeS biomineral transformations: Geophysical Research Letters, 34.

Slater, L. D., D. Ntarlagiannis, F. D. Day-Lewis, K. Mwakanyamale, R. J. Versteeg, A. Ward, C. Strickland, C. D. Johnson, and J. W. Lane Jr., 2010, Use of electrical imaging and distributed temperature sensing methods to characterize surface water–groundwater exchange regulating uranium transport at the Hanford 300 Area, Washington: Water Resources Research, 46.

Soueid Ahmed, A., A. Revil, S. Byrdina, A. Coperey, L. Gailler, N. Grobbe, F. Viveiros, C. Silva, D. Jougnot, A. Ghorbani, C. Hogg, D. Kiyan, V. Rath, M. J. Heap, H. Grandis, and H. Humaida, 2018, 3D electrical conductivity tomography of volcanoes: Journal of Volcanology and Geothermal Research, 356, 243–263.

Soupios, P., N. Papadopoulos, I. Papadopoulos, M. Kouli, F. Vallianatos, A. Sarris, and T. Manios, 2007, Application of integrated methods in mapping waste disposal areas: Environmental Geology, 53, 661–675.

Steiner, M., T. Katona, J. Fellner, and A. Flores Orozco, 2022, Quantitative water content estimation in landfills through joint inversion of seismic refraction and electrical resistivity data considering surface conduction: Waste Management, 149, 21–32.

Tejero-Andrade, A., G. Cifuentes, R. E. Chávez, A. E. López-González, and C. Delgado-Solórzano, 2015, L- and CORNER-arrays for 3D electric resistivity tomography: an alternative for geophysical surveys in urban zones: Near Surface Geophysics, 13, 355–367.

Tsourlos, P., N. Papadopoulos, M.-J. Yi, J.-H. Kim, and G. Tsokas, 2014, Comparison of measuring strategies for the 3-D electrical resistivity imaging of tumuli:

Journal of Applied Geophysics, 101, 77–85.

Van Hoorde, M., T. Hermans, G. Dumont, and F. Nguyen, 2017, 3D electrical resistivity tomography of karstified formations using cross-line measurements: Engineering Geology, 220, 123–132.

Vinegar, H. J., and Waxman, M. H., 1984, Induced polarization of shaly sands: Geophysics, 49, 1267–1287.

Wainwright, H. M., A. Flores Orozco, M. Bücker, B. Dafflon, J. Chen, S. S. Hubbard, and K. H. Williams, 2016, Hierarchical Bayesian method for mapping biogeochemical hot spots using induced polarization imaging: Water Resources Research, 52, 533–551.

Ward, S. H., 1990, Resistivity and Induced Polarization Methods, in Ward, S. H., eds., Geotechnical and environmental geophysics: Society of Exploration Geophysicists, 147–189.

Waxman, M. H., and Smits, L. J. M., 1968, Electrical conductivities in oil-bearing shaly sands: Society of Petroleum Engineers Journal, 8, 107–122.

Weigand, M., A. Flores Orozco, and A. Kemna, 2017, Reconstruction quality of SIP parameters in multi-frequency complex resistivity imaging: Near Surface Geophysics, 15, 187–199.

Weller, A., L. Slater, A. Binley, S. Nordsiek, and S. Xu, 2015, Permeability prediction based on induced polarization: Insights from measurements on sandstone and unconsolidated samples spanning a wide permeability range: Geophysics, 80, no. 2, D161–D173.

Weller, A., L. Slater, S. Nordsiek, and D. Ntarlagiannis, 2010, On the estimation of specific surface per unit pore volume from induced polarization: A robust empirical relation fits multiple data sets: Geophysics, 75, no. 4.

Wilkinson, P., J. Chambers, S. Uhlemann, P. Meldrum, A. Smith, N. Dixon, and M. Loke, 2016, Reconstruction of landslide movements by inversion of 4-D electrical resistivity tomography monitoring data: Geophysical Research Letters, 43.

Wong, J., 1979, An electrochemical model of the induced-polarization phenomenon in disseminated sulfide ores: Geophysics, 44, no. 7, 1245–1265.

Zisser, N., A. Kemna, and G. Nover, 2010, Dependence of spectral-induced polarization response of sandstone on temperature and its relevance to permeability estimation: Journal of Geophysical Research, 115.